CZECH TECHNICAL UNIVERSITY IN PRAGUE

FACULTY OF NUCLEAR SCIENCES AND PHYSICAL ENGINEERING

Department of Physics

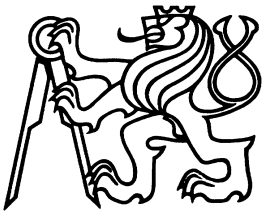

Low Proton Flux Measurements at the U-120M Cyclotron for Radiation Hardness Studies

MASTER'S THESIS

Author: **Kamila Vysoká**
Supervisor: **RNDr. Filip Křížek, Ph.D.**
Academic year: **2015/2016**

Prehlásenie

Prehlasujem, že som svoju diplomovú prácu vypracovala samostatne a použila som len literatúru a publikácie uvedené v priloženom zozname.

Nemám závažný dôvod proti použitiu tohoto školského diela v zmysle §60 Zákona č.121/1200Sb., o autorskom práve, o právach súvisiacich s autorským právom a o zmene niektorých zákonov (autorský zákon).

V Prahe dňa ....

Název práce: **Měření nízkých toků protonů na cyklotronu U-120M pro účely testů radiační odolnosti**
Autor: Kamila Vysoká

Obor: Experimentální jaderná a částicová fyzika
Druh práce: Diplomová práca

Vedúcí práce: RNDr. Filip Křížek, Ph.D.
Ústav jaderné fyziky, v.v.i. AV ČR

Abstrakt:

V nadchádzajúcich rokoch 2019–2020 sa kolaborácia ALICE vo výskumnom centre CERN pripravuje na upgrade vnútorného dráhoveho detektoru (ITS). Materiál a elektronické súčiastky, ktoré majú byť použité v novom detektore musí byť testované, či vydržia očakávanú celkovú dávku ožiarenia, ktorá bude absorbovaná v priebehu prevádzky ITS. Česká skupina pracujúca na ALICE využíva protónový tok z isochronného cyklotrónu U-120M v Ústave jaderné fyziky AV ČR v Řeži na vykonanie skúšky radiačnej odolnosti niektorých jeho zložiek, napr. FPGA a káblov. On-line parametre protónového zväzku sú sledované pomocou ionizačnej komory 30010 PTW. Táto práca opisuje postup, ktorý bol použitý na nájdenie vzťahu medzi prúdom nameraným ionizačnou komorou a protónovým tokom meraným detektorom Timepix. K lepšiemu pochopeniu získaných kalibračných kriviek sme použili simulácie z Geant4 a SRIM.

Kľúčové slová: Testovanie radiačnej odolnosti, upgrade ITS, ALICE, protónové žiarenie, prechod ťažkých nabitých častíc látkou, isochronný cyklotron U-120M, ionizačná komora, Timepix, energetický degrader, Geant4, SRIM.

Title: **Low Proton Flux Measurements at the U-120M Cyclotron for Radiation Hardness Studies**

Author: Kamila Vysoká

Abstract:

In the upcoming years 2019–2020, the ALICE collaboration at CERN prepares an upgrade of the Inner Tracker Detector (ITS). Material and electronic components to be used in the new detector have to be tested whether they sustain the expected total radiation dose which will be accumulated during the ITS operation. The Czech ALICE group uses the proton fluxes provided by the isochronous cyclotron U-120M at the Nuclear Physics Institute of the Czech Academy of Sciences in Řež to perform the necessary tests of the radiation hardness of some ITS components, e.g., FPGAs and cables. The on-line parameters of the proton beam are monitored with the ionization chamber 30010 PTW. The thesis describes a procedure which was used to find the relation between the ionization current measured by the chamber and the proton flux measured by the Timepix detector. To gain a better understanding of the obtained calibration curves we employ the Geant4 and SRIM simulations.

Keywords: Radiation hardness testing, ITS upgrade, ALICE, proton irradiation, proton interaction in matter, isochronous cyclotron U-120M, ionization chamber, Timepix, energy degrader, Geant4, SRIM.

Acknowledgement

I would like to thank to my supervisor Filip Křížek for his guidance and useful comments which greatly helped to produce this thesis. I also want to thank to the whole Czech ALICE group and especially to Jozef Ferencei, Tomáš Vaňát and Peter Príbeli for useful advice and help. I would like to thank to IEAP for providing the Timepix and especially to Dr. Carlos Granja for support. I am grateful to the NPI cyclotron management and crew for great performance and support (CANAM project 60). And last but certainly not least I would love to thank to my beloved husband Jan Vysoký for his endless support and infinitely kind words of encouragement.

Contents

Introduction

Ionizing radiation is a natural part of our daily lives. However, in some areas of research and applications, we are confronted with doses that are several orders of magnitude higher than the doses which we are normally exposed to. Such areas are not only medicine, nuclear energetics, space program, and particle research but also, e.g., the aviation. Radiation damages materials and tissues by changing their structure and physical properties. Therefore, it is necessary to know what is the response of the given material or device to different types and levels of radiation. This is called radiation hardness testing.

Nowadays, there is a great push toward the miniaturization of the size of different material structures used in electronics and computers. Inevitably we are getting to the situation when the new devices are getting more and more sensitive to the influence of ionizing particles. For safety measures the computers and electronics which are expected to be exposed to higher radiation doses are heavily tested to reveal possible errors that might occur while operation in real life. In the cases where accurate computer calculations are important for the safety of people and property, computational systems are multiplied and make calculations independently. The final decision is then obtained from a majority-voting system to produce a single output. In such cases we speak about Tripple or N-modular redundancy. The typical examples where this concept is used are the navigation of airplanes Airbus [1] or computer systems in spacecrafts.

The ALICE experiment [2] (A Large Ion Collider Experiment) at the CERN (European Organization for Nuclear Research) LHC accelerator (Large Hadron Collider) is going to upgrade its Inner Silicone Tracker detector (ITS) [3]. Besides precise tracking this detector has a role to determine a position of the primary and secondary vertices of particles leaving the interaction point and to provide a fast triggering signal. The region close to the beam pipe is, however, exposed to a large radiation load. Consequently, there might be a non-negligible radiation damage induced on the used electronics and other parts of the detector. Therefore, it is important to test the radiation hardness of all detector parts and to search for radiation tolerant technologies and materials. For this purpose the Czech ALICE group uses the proton fluxes provided

by the isochronous cyclotron U-120M at the Nuclear Physics Institute of the Czech Academy of Sciences in Řež [4]. So far the group has tested radiation hardness of various types of Field-Programmable Gate Arrays (FPGA) [5] and wires, which are intended to be used for the new ITS detector. The main purpose is to determine what is the maximum dose that individual components can accept without a negative effect on their function. To determine this dose, it is necessary to know relatively accurately what proton flux is delivered by the cyclotron at given proton beam energy.

The tests of radiation hardness require very low proton fluxes which are far below what can be measured by the standard tools available to the cyclotron operators. Hence, it was necessary to develop other methods to determine the instantaneous proton flux with sufficient accuracy. For this purpose we use a commercial ionization chamber from PTW Freiburg (German: Physikalisch-Technische Werkstätten) [6].

The main goals of this thesis were the following:

1. Provide a conversion factor between the current measured by the ionization chamber and the proton flux measured by the Timepix detector [7].

2. Compare the measured data with simulations done by Geant4 (GEometry ANd Tracking) and SRIM (Stopping and Range of Ions in Matter) to get better understanding how protons interact in various parts of the set-up.

Thesis is organized as follows:

The opening chapter of this thesis deals with the interaction of protons in matter. Necessary physical and dosimetric quantities are being introduced. Further we briefly describe the SRIM and Geant4 software which are used to model interactions of ionization radiation in matter. The chapter 2 summarizes details of the experimental set-up used for the radiation hardness tests, the detectors employed (Timepix and ionization chamber), the isochronous cyclotron U-120M and the energy degrader. The chapter 3 deals with the analysis of the experimental data and reviews physical conditions during the experiment. Here one finds also the major achievement of this work, the correlation between the proton flux measured by the Timepix detector and the current measured by the ionization chamber. The chapter 4 discusses the simulations of the set-up performed using Geant4 and SRIM. The simulations are used to assess how various components of the set-up influence the incoming proton beam. In the last chapter we conclude and summarize the achieved results.

Chapter 1

Proton Interaction in Matter

Detail understanding of processes which occur when a particle penetrates through matter is in particle physics very important. It helps to come up with working detector design and is needed to assess corresponding detector efficiency and resolution. In this section we, therefore, summarize some basics of the proton interaction with matter. We will focus on the interactions that dominate in the energy regime accessible with the beams delivered by the isochronous cyclotron U-120M, i.e., the kinetic energies up to 37 MeV. In this particular energy domain the dominant energy loss of the proton projectile is caused by the Coulomb interaction of the proton with electrons in the target material. Since the proton is much heavier than the electron, such collisions do not change the direction of the proton momentum significantly. The proton can be thus considered as a heavy charged particle. Hence we can use the results of theory that were derived for such a limiting case.

The protons can interact in matter by these processes [8]:

1. inelastic scattering with atomic electrons of the target material,
2. elastic scattering with nuclei of the target material,
3. nuclear reaction,
4. Cherenkov radiation,
5. bremsstrahlung.

The last two processes in the list are not relevant for the energy loss in our energy range. The process with the highest probability to occur is the proton interaction with atomic electrons. It can either excite or ionize atoms in the matter depending on the momentum transfer that happens in the inelastic collision. The second in the list is the process of interactions with nuclei.

Usually, in such a collision, only a small part of the projectile proton energy is transferred to the recoil of the target nucleus since often the target nucleus has larger mass than the projectile proton. When the proton has energy high enough to overcome the Coulomb barrier of a nucleus it can induce a nuclear reaction. Due to the finite range of the nuclear force and tiny dimensions of nuclei, the probability of this process is much smaller compared to the electromagnetic interaction.

1.1 Energy Loss

The basic quantity that describes the energy loss of a heavy charged particle such as the proton in matter is the so-called *stopping power* $-\frac{\mathrm{d}E}{\mathrm{d}x}$. It gives the energy loss of the projectile particle per a unit path length traversed in the material. As all collisions that the particle undergoes in given material can be viewed as random processes with the rates driven by the laws of Quantum Mechanics, the resulting total energy loss for each projectile is also a random number. Nevertheless, the mean $-\frac{\mathrm{d}E}{\mathrm{d}x}$ can be to a good approximation described by the Bethe-Bloch formula [9], which parameterizes the mean stopping power in terms of quantities related to the properties of the considered material and the incoming particle. The Bethe-Bloch formula reads

$$-\frac{1}{\rho}\left\langle\frac{dE}{dx}\right\rangle = Kz^2\frac{Z}{A}\frac{1}{\beta^2}\left[\frac{1}{2}\ln\frac{2m_ec^2\beta^2\gamma^2T_{max}}{I^2}-\beta^2-\frac{\delta(\beta\gamma)}{2}\right], \tag{1.1}$$

where ρ is the material density, z is the charge of the incident particle, Z is the atomic number of the material, A is the atomic mass of the material, $\beta=\frac{v}{c}$ is the ratio of the incident particle velocity and the speed of light, m_e is the mass of the electron, $\gamma=(1-\beta)^{-\frac{1}{2}}$ is the Lorentz factor, T_{max} is the maximum transferred kinetic energy to a free electron in a single collision, I is the mean excitation energy and $\delta(\beta\gamma)$ is the correction for the effects caused by density. The constant K is equal to

$$K = 4\pi N_A r_e^2 m_e c^2\,, \tag{1.2}$$

where N_A is the Avogadro constant and $r_e=\frac{e^2}{4\pi\varepsilon_0 m_e c^2}$ is the classical radius of the electron [10].

The Bethe-Bloch formula was derived under several assumptions, e.g., the projectile particle moves much faster than the electrons on their orbits and hence the electrons are considered to be initially at rest, the projectile particle does not change its charge, the projectile energy is transferred only to the atomic electrons.

Figure 1.1 shows the stopping power of the muon in copper as a function of muon $\beta\gamma$ or momentum. The Bethe-Bloch curve for the proton in copper would look similar. The proton with a kinetic energy of 34 MeV has $\beta = 0.262$ and $\beta\gamma = 0.272$.

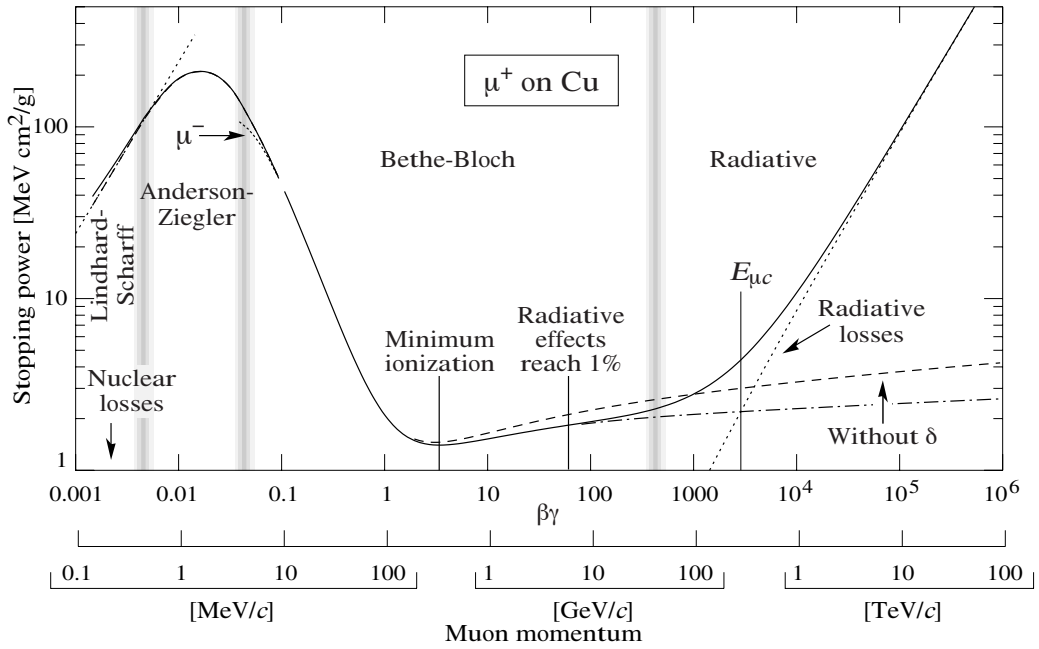

Figure 1.1: Stopping power $-\frac{1}{\rho}\langle\frac{\mathrm{d}E}{\mathrm{d}x}\rangle$ for the muon in copper as a function of the muon $\beta\gamma$ or momentum. Taken from [10].

The Bethe-Bloch curve has a pronounced minimum at $\beta\gamma \sim 3$. For smaller $\beta\gamma$ the decreasing energy of the projectile particle leads to the increase of its stopping power. This behavior is driven by the β^{-2} dependence of $\langle-\frac{\mathrm{d}E}{\mathrm{d}x}\rangle$ in (1.1). The particle will thus have the largest energy losses close to the end of its trajectory. The dependence of the stopping power on the path length is often called as the Bragg curve, see Figure 1.3. The Bethe-Bloch curves for the protons in different materials are in Figure 1.2. The trend of the curves is very similar. The observed spread between the curves shows the residual differences that remain after the factorization with the density of the target material.

Close to the end of the path assumptions under which the Bethe-Bloch formula was derived are no longer valid. E.g. for the projectile particles with $\beta\gamma < 0.1$ it is observed that the stopping power of the positively and the negatively charged projectiles differs. This is the so-called *Barkas-Anderson effect* [11], which can be explained as follows. When the projectile particle is sufficiently slow, the collision time gets longer. The atomic electrons can

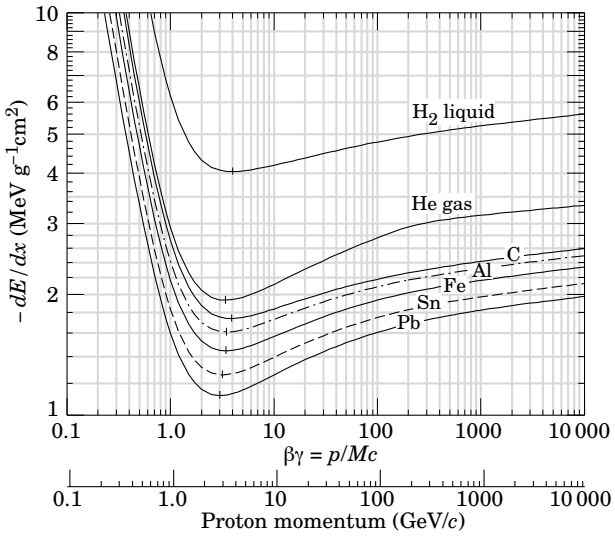

Figure 1.2: Mean energy loss rate of the proton in liquid hydrogen, helium gas, carbon, aluminum, iron, tin, and lead. Taken from [10].

then move considerably during the interaction. When this happens, the positively charged particles should have a smaller effective impact parameter which results to an increase of the transferred energy. For the negatively charged projectile particles the situation is the opposite. At even lower values of $\beta\gamma$ the projectile particle can e.g. capture an electron and reduce its charge which leads to a reduction of $\langle -\frac{\mathrm{d}E}{\mathrm{d}x} \rangle$.

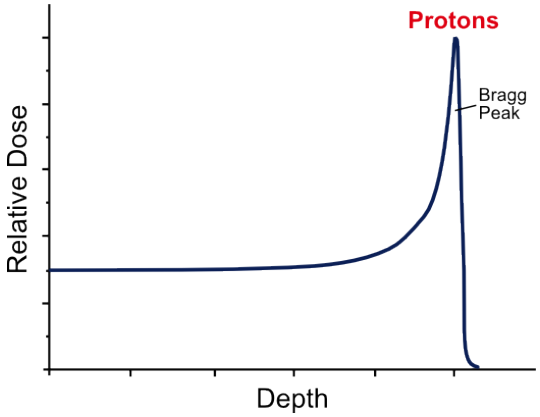

Figure 1.3: Illustration of the Bragg curve. Radiation dose as a function of the depth traversed in the target material for a proton beam. Taken form [12].

The probability that a heavy ionizing particle reaches a given depth in material is illustrated in Figure 1.4. We see that the number of particles in

the beam stays nearly constant until reaching certain depth beyond which the survival probability tends to decrease. Common quantities used to express the reach of particles in the material are called the mean range and the extrapolated range. The extrapolated range is usually obtained by means of a linear extrapolation of the first half of the drop in the transition range.The mean range is obtained as the mean value of the normal distribution which in the first approximation describes the distribution of ranges for identical particles with the same initial energy. The concept of the range is, however, applicable only in the case when the mean nuclear interaction length is larger than the mean range [13].

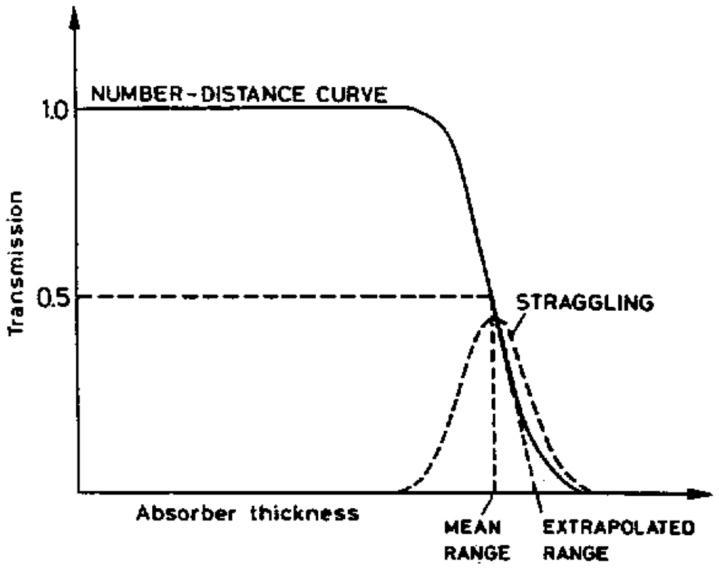

Figure 1.4: The distribution of ranges (dashed line) has a Gaussian form. The plot illustrates also the corresponding mean and the extrapolated range. Taken from [8].

We can estimate the range based on the formula for stopping power. Integrating the inverse of (1.1) in the energy range from the initial particle energy T_0 down to zero kinetic energy we get

$$R'(T_0) = \int_{T_0}^{0} \left(-\frac{\mathrm{d}E}{\mathrm{d}x}\right)^{-1} \mathrm{d}E. \tag{1.3}$$

This formula, however, assumes that the particle trajectory is straight. To compensate for this approximation in practice one generally uses a similar semi-empirical formula

$$R(T_0) = R_0(T_{\min}) + \int_{T_0}^{T_{\min}} \left(-\frac{\mathrm{d}E}{\mathrm{d}x}\right)^{-1} \mathrm{d}E, \tag{1.4}$$

where $T_{\min}$ is the minimal energy at which $\frac{\mathrm{d}E}{\mathrm{d}x}$ is valid and $R_0(T_{\min})$ is an empirical constant, which parameterizes projectile behavior at low energies [13].

1.2 Multiple Coulomb Scattering

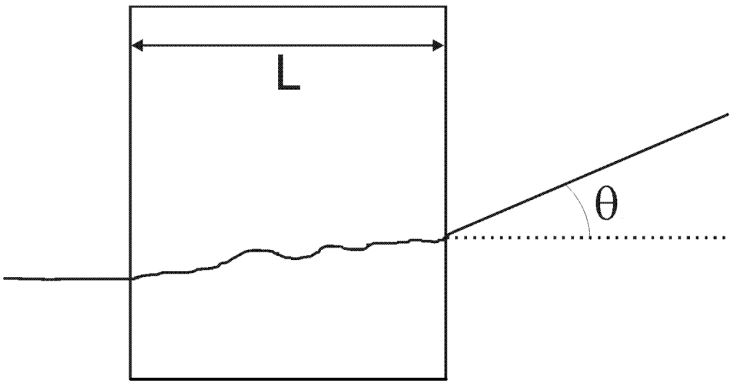

Figure 1.5: Effects of multiple Coulomb scattering on the projectile particle traveling through material of thickness L. The deflection angle from the original direction is denoted by θ. Taken from [14].

A trajectory of a particle traversing through a material is usually deflected by several Coulomb scatterings of the nuclei and electrons, see Figure 1.5. Deflections caused by the nuclei are typically larger because they are heavier than the electrons and have greater charge. The resulting angular distribution of the scattered particles gets contributions from

1. Single scattering. If the probability for more than one scattering is negligible, as it is the case for a thin layer, the projectile angular distribution is given by the Rutherford formula

$$\frac{\mathrm{d}\sigma}{\mathrm{d}\Omega} = \left(\frac{Zz\alpha\hbar c}{T}\right)^2 \sin^{-4}\left(\frac{\theta}{2}\right), \tag{1.5}$$

   where Z and z are the charges of the projectile particle and the target material nucleus measured in the units of the elementary charge $|e|$, α is the fine-structure constant, $\hbar$ is the reduced Planck constant, c is the speed of light in vacuum, T is the kinetic energy of the incident particle and θ is the deflection angle from the initial direction [13].

2. Plural scattering. It can be applied if the number of consecutive scatterings is smaller than 20. This case is more complicated than the others since the simple Rutherford formula is not applicable and simultaneously the multiplicity of consecutive scatterings is too small to be handled statistically. Formulas that describe angular scattering in this domain are given e.g. in [15].

3. Multiple scattering. This is the most commonly used case. Theoretical description of this regime assumes that the projectile undergoes many scatterings but the energy loss in one collision is small. The distribution of the scattering angle of the projectile particles that underwent multiple coulomb scattering follows a Gaussian distribution centered at zero with the standard deviation

$$\frac{\sigma_\theta}{\sqrt{2}} = \frac{13.6\,\mathrm{MeV}}{\beta c p} z \sqrt{\frac{L}{X_0}} \left[1 + 0.038 \ln\left(\frac{L}{X_0} \right) \right], \tag{1.6}$$

where $sigma_\theta$ represents the width of the two dimensional symmetrical Gaussian distribution, β is the speed of the incident particle divided by the speed of light c, p is the projectile particle momentum, z is the charge of the incident particle the units of the elementary charge $|e|$, L is material thickness and X_0 is a radiation length which can be found in tables e.g. [16].

In Figure 1.6 we show an example of the angular distribution of electrons scattered on a golden foil. Small angle deflections are dominantly populated by the multiple coulomb scattering. At the large angles, contributions of single coulomb scattering prevail as in this region the less steep power-law decrease of the Rutherford formula wins over the much steeper exponential drop of the Gaussian distribution which describes the multiple Coulomb scattering. Connection between those regimes was provided by the theory of Gert Molière [17].

1.3 Nuclear Reactions

The proton colliding with a nucleus is able to induce a nuclear reaction. The probability that the proton induces a nuclear reaction is however several orders of magnitude smaller when compared with the probability that it undergoes Coulombic scattering with an electron or nucleus. Let us note that the nuclear strong force has only a short range and that the size of nuclei is small when compared to typical inter-atomic distances in the material. In addition the Coulombic barrier tends to repel the protons from the reach of the nuclear potential.

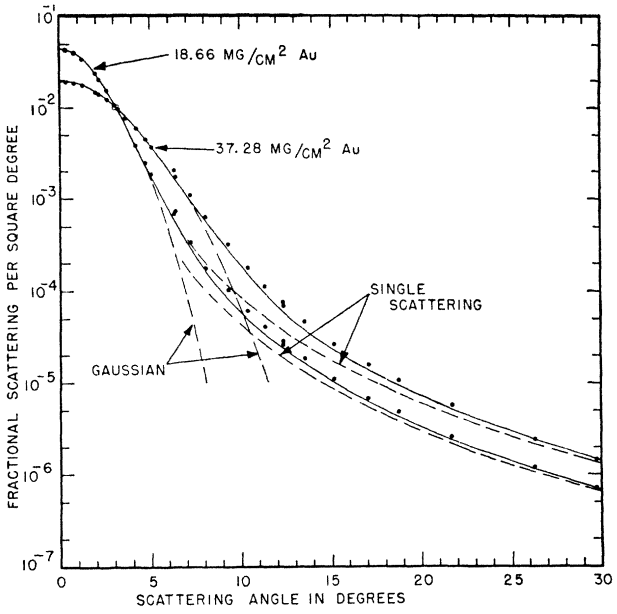

Figure 1.6: Angular distribution of 15.7 MeV electrons on a golden foil in the range of deflection angles 0° to 30°. The dashed lines mark the Gaussian approximation at small angles and the single scattering approximation at large angles. The solid lines represent the Molière's approximation, taken from [18].

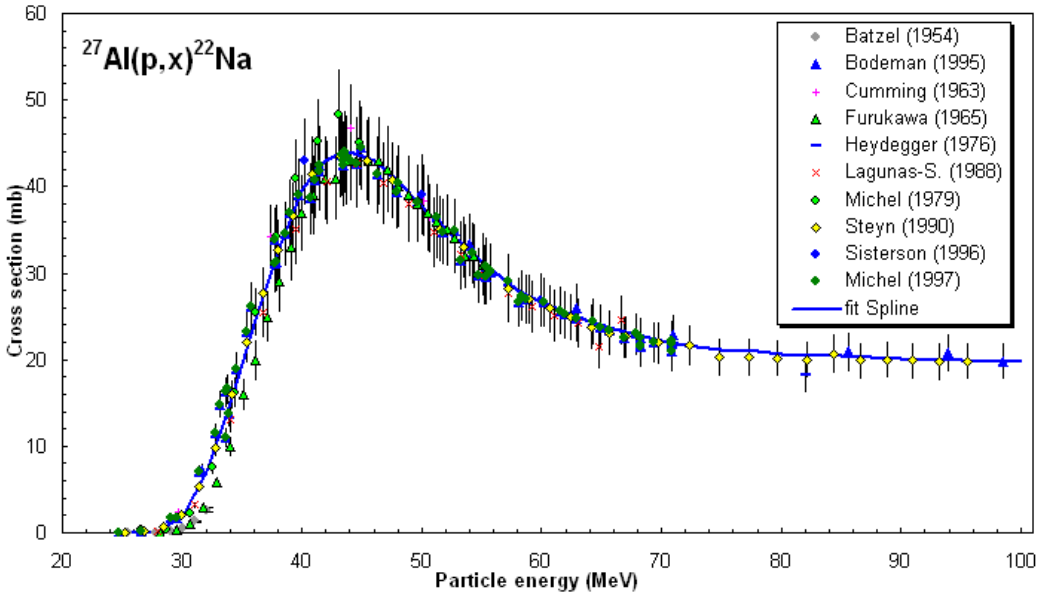

Figure 1.7: Cross section for the reaction ^{27}Al(p,X)^{22}Na as a function of the projectile proton energy, taken from [19].

One of the basic quantities describing particle interaction is the *cross section*. It is related to the probability that a given reaction will occur. The cross-section can be defined as

$$\sigma = \frac{Y}{\rho_n \cdot \phi \cdot t_{irr}} \tag{1.7}$$

where Y is the reaction yield, ρ_n is the number density of the target particle, ϕ is the proton flux, and t_{irr} is the time of irradiation [13]. The proton flux gives the number of protons that fly through a unit area per a unit of time. The proton flux integrated over some time interval is called the fluence[20]. Nuclear reaction cross sections are generally energy dependent. In Figure 1.7 we show as an illustration the case of the reaction ^{27}Al(p,X)^{22}Na. Since the protons that traverse though a material lose energy, the probability to induce a nuclear reaction changes accordingly.

1.4 Dose

Radiation damage induced by ionizing particles in material is usually quantified by the ionization dose. The ionization dose is defined as the absorbed energy per unit mass,

$$D = \frac{\mathrm{d}E}{\mathrm{d}m}. \tag{1.8}$$

The unit of the ionization dose is called gray. The body receives an ionization dose of one gray when it absorbs one joule of energy from the incoming radiation per one kilogram of its mass. In common practice, the ionization dose is often expressed using another unit called rad [8], which is related to the gray as $100\,\mathrm{rad} = 1\,\mathrm{Gy}$.

Although the absorbed energy is related to the damage induced in material, this relation is not simple. For instance the same bodies irradiated by 37 MeV protons and 7 TeV protons and obtaining the same dose will exhibit different material damage. This follows from the fact that the cross section of the proton interaction with nuclei is energy dependent [21].

1.5 SRIM

Stopping and Range of Ions in Matter (SRIM) [22] computer program was developed to calculate interactions of ions in matter. The authors of this program are James F. Ziegler and Jochen P. Biersack who initially released SRIM in 1983 as a DOS based program. In 1989, it was adapted for Windows and since then it is continuously upgraded.

To calculate the propagation of a heavy ionizing particle through matter, SRIM employs the Monte Carlo based approach. Ion-atom collisions are treated based on the results of quantum mechanical calculations. A binary collision approximation is assumed and the corresponding impact parameter is varied randomly.

As the input parameters of SRIM one specifies the type of ion an its energy which can be in the range 10 eV–2 GeV. SRIM can describe only simple experimental geometries consisting of layers. For each layer we can choose material and thickness. We utilize the SRIM version 1.5.

1.6 Geant4

Geant4 [23] is a Monte Carlo based simulation code to calculate particle transport through matter. In contrast to SRIM, Geant4 is more versatile and variable. It allows to simulate wider set of processes with more types of incident particles over broader energy range. On top of that Geant4 supports implementation of very complex geometries.

The program is based on object oriented programming (C++) and was developed by CERN . We utilize the Geant4 version 4.10.

Chapter 2

Experimental Aparature

In this chapter we describe the experimental set-up which was used in the measurement. Namely we will describe the isochronous cyclotron U-120M, the ionization chamber PTW 30010, the Timepix and the energy degrader.

2.1 Isochronous Cyclotron U-120M

A cyclotron is a circular particle accelerator. It was invented and first constructed by Ernest Lawrence in 1932 [24]. The scheme of a typical cyclotron is shown in Figure 2.1. A central vacuum chamber with two electrodes shaped like a half of hollow cylinder is placed between the poles of a strong electromagnet. The electrodes are called Dees. The Dees are insulated form each other and are placed such that there is a narrow gap in between them. The polarity of the Dees is changed periodically with a frequency of order of 20 MHz.

Charged particles are injected to the vacuum chamber at the center of the accelerator. Due to the Lorentz force particles follow a circular trajectory inside the Dee until they reach its edge. In the gap between the Dees particles are accelerated by the electric field. The particles with increased speed now travel with the same angular velocity on a circular trajectory having a grater radius. The cyclotron accelerates particles only when the frequency and the phase of the electrical field in the gap are the same as the frequency and the phase of particles on their orbit. The radius of particle orbit follows from the equilibrium between the Lorentz force and centrifugal force.

$$Bqv = \frac{mv^2}{r}, \tag{2.1}$$

where q is particle charge, B denotes magnetic field, v is particle velocity, m is particle mass and r is the radius of the circular trajectory. Expressing the

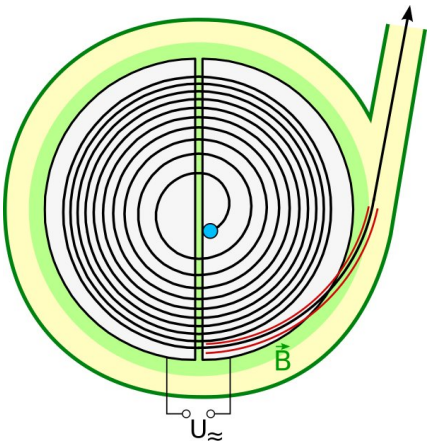

Figure 2.1: Scheme of a cyclotron with a trajectory of an accelerated particle and its ejection through a beam line [25].

velocity as

$$v = 2\pi r f \tag{2.2}$$

we obtain the formula for the cyclotron frequency [13]

$$f = \frac{Bq}{2\pi m}\,. \tag{2.3}$$

The measurements discussed in this thesis were done on the proton beam provided by the isochronous cyclotron U-120M at the Nuclear Physics Institute of the Czech Academy of Sciences in Řež, see Figure 2.2. Let us point out that there is one slight difference in the construction of the isochronous cyclotron U-120M with respect to the usual cyclotron design described above. The Řež cyclotron has just one Dee electrode. The role of the second Dee is taken by the walls of the vacuum chamber which is grounded [26].

The arrangement of the cyclotron U-120M allows to accelerate positively charged light ions H^+, D^+, $^3He^{+2}$ and α and negatively charged ions H^- and D^-. Each of the acceleration modes requires different ejection mechanism. The positive mode accelerating positively charged ions uses a magnetic kicker and three sections of electrostatic deflection systems, see the left hand side panel in Figure 2.3. The negative mode accelerates negatively charged ions in the same direction as positive mode. The negative ions are stripped of the valence electrons by passing through a $1\,\mu$m thick carbon stripping foil. The Lorentz force then automatically bends the beam of now positive ions out of the vacuum chamber and directs it to a short beam line, see the left hand side in Figure 2.3 [4]. The short beam line is equipped with a series of quadrupole focusing magnets and is terminated with a $55\,\mu$m thick aluminum beam pipe exit window which separates the internal cyclotron vacuum from

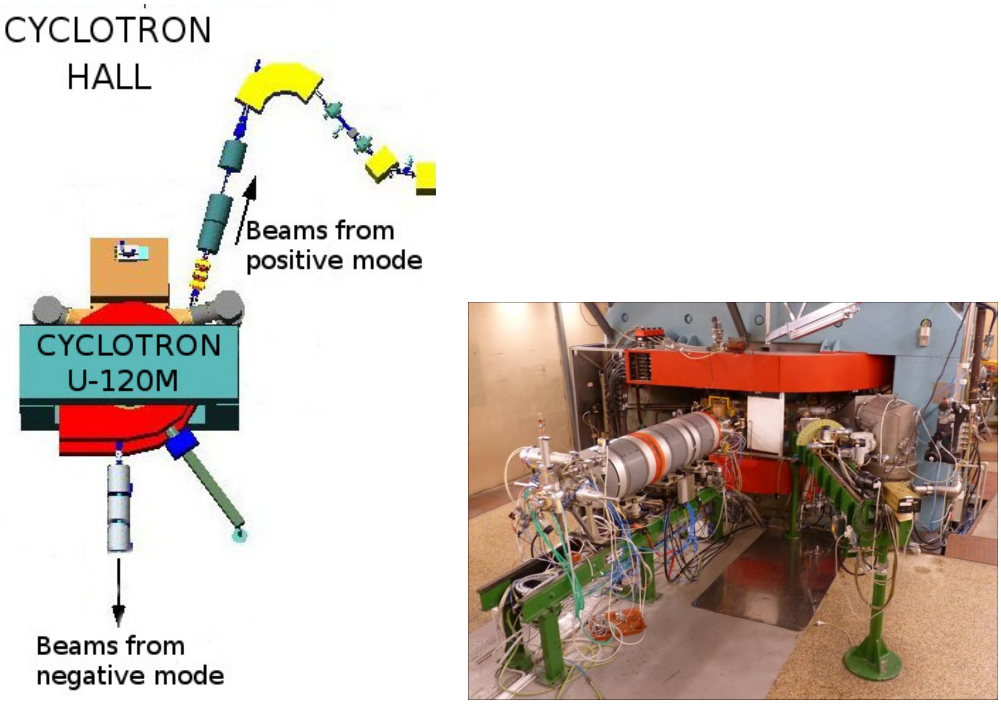

Figure 2.2: Left: Scheme of the isochronous cyclotron U-120M together with the beam lines for the positive and the negative mode. Right: The negative mode beam line from the isochronous cyclotron U-120M. Taken from [4].

the surrounding air. The negative mode has larger efficiency of the beam extraction because the positive mode suffers from significant beam losses on the electrostatic deflectors. On the other hand it has a little bit worse uncertainty in the delivered beam energy. For the negative mode this uncertainty is of order $\sim 0.25\,\mathrm{MeV}$ [26]. The setup for our measurement was installed on the output beam line from the negative mode.

The time structure of the beam from the U-120M isochronous cyclotron can be described as follows. The basic $\sim 25\,\mathrm{MHz}$ cyclotron radio frequency separates ions into 40 ns long beam buckets. The injection of particles from the ion source into the cyclotron is, however, initiated by a much lower frequency 150 Hz pulse having a period of 6.667 ms. This pulse has an adjustable length, the so-called *duty factor*. When accelerating protons to the top energies (35 MeV), the duty factor can take only 5 to 20 % of the 6.667 ms period. The situation is illustrated in Figure 2.4.

Parameters of the accelerated and extracted beams (energy range and the maximal current) that can be delivered by the U-120M isochronous cyclotron are listed in Table 2.1. For the purpose of radiation hardness testing we need H^- beams which have eight orders of magnitude lower current ($I \approx 100\,\mathrm{fA}$)

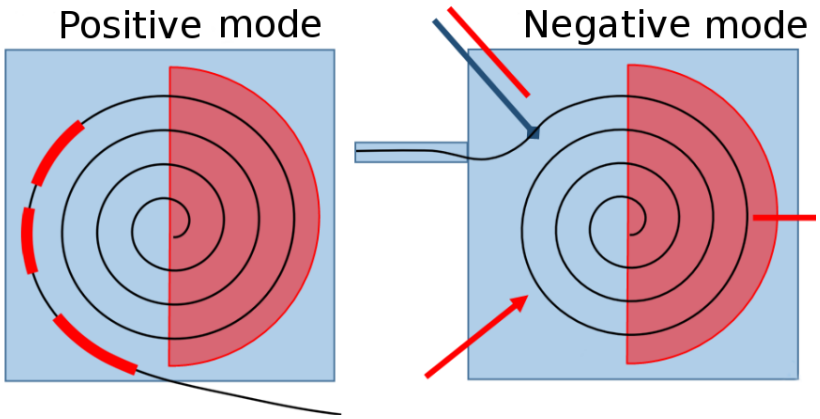

Figure 2.3: The positive and the negative mode of the U-120M isochronous cyclotron. The Dee electrod is marked by the red semi-circle. In the positive mode the beam is extracted by means of three electrostatic deflectors marked in red. In the negative mode the beam is extracted using a stripping foil placed in the upper left corner of the figure and marked with dark blue color.

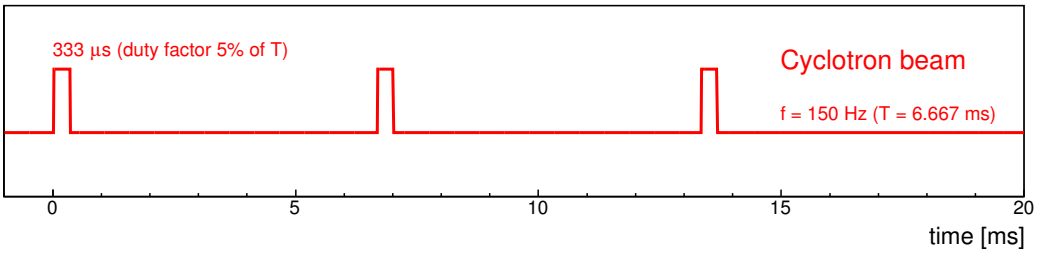

Figure 2.4: Time structure of the beam delivered by the U-120M isochronous cyclotron. The figure illustrates the situation corresponding to case when the duty factor is 5 %, i.e. protons are accelerated throughout 333 μs of the 6.667 ms period. Each 333 μs pulse consists of 40 ns long beam buckets.

than the maximal achievable current. The reduction of the beam current can be accomplished by several different ways:

1. reducing the duty factor,
2. increasing gas pressure in the ion source,
3. displacing the ion source exit window with respect to the input window to the vacuum chamber,
4. turning off the beam focusing quadrupole magnets,
5. inserting a collimator or a beam probe into the beam.

Out of the listed possibilities it is only the first one that does not change the transverse beam profile.

Ion	E [MeV]	I_{max} [μA]
H^+	6 - 25	5
H^-	6 - 37	50 - 35
D^+	12 - 20	5
D^-	11 - 20	35 - 20
$^3He^{+2}$	18 - 52	2
α	24 - 38	5

Table 2.1: Range of kinetic energies and the maximal current for given ion beam. Data correspond to the external beams from the isochronous cyclotron U-120M. Taken from [4].

2.2 Energy Degrader

The energy degrader allows to change the beam energy or to interrupt the irradiation without the need to stop the cyclotron. This has the advantage that conditions at which the cyclotron operates and the resulting beam parameters are kept stable throughout the whole irradiation. The energy degrader consists of five aluminum plates of different thickness, which can be instantly placed into the beam by a remotely operated pneumatic system. The first plate has a width of 8 mm which is sufficient to stop the 35 MeV proton beam completely. The thickness of the other four plates is given in Table 2.2. Their role is to change the beam energy. In addition, they make the beam profile wider which helps to achieve better spatial homogeneity of the beam at the irradiation spot.

Plate	Set A	Set B
5	(4.19±0.01) mm	(3.88±0.02) mm
4	(2.05±0.01) mm	(1.92±0.01) mm
3	(1.09±0.02) mm	(0.86±0.03) mm
2	(0.57±0.06) mm	(0.49±0.02) mm

Table 2.2: Thicknesses of degrader plates in two sets that are available. The consecutive number of each plate gives its position from the end of the beam line. Our measurement was carried out using the set A. All measured data are recorded in Table A.1

The energy degrader is mounted at the end of the cyclotron beam line from the negative mode, see Figure 2.5. The degrader performance will be discussed

farther in Chapter 3. In Chapter 4 we present the detailed Geant4 simulation of the full experimental setup with the degrader, e.g., we show how different configurations of degrader plates change the beam energy.

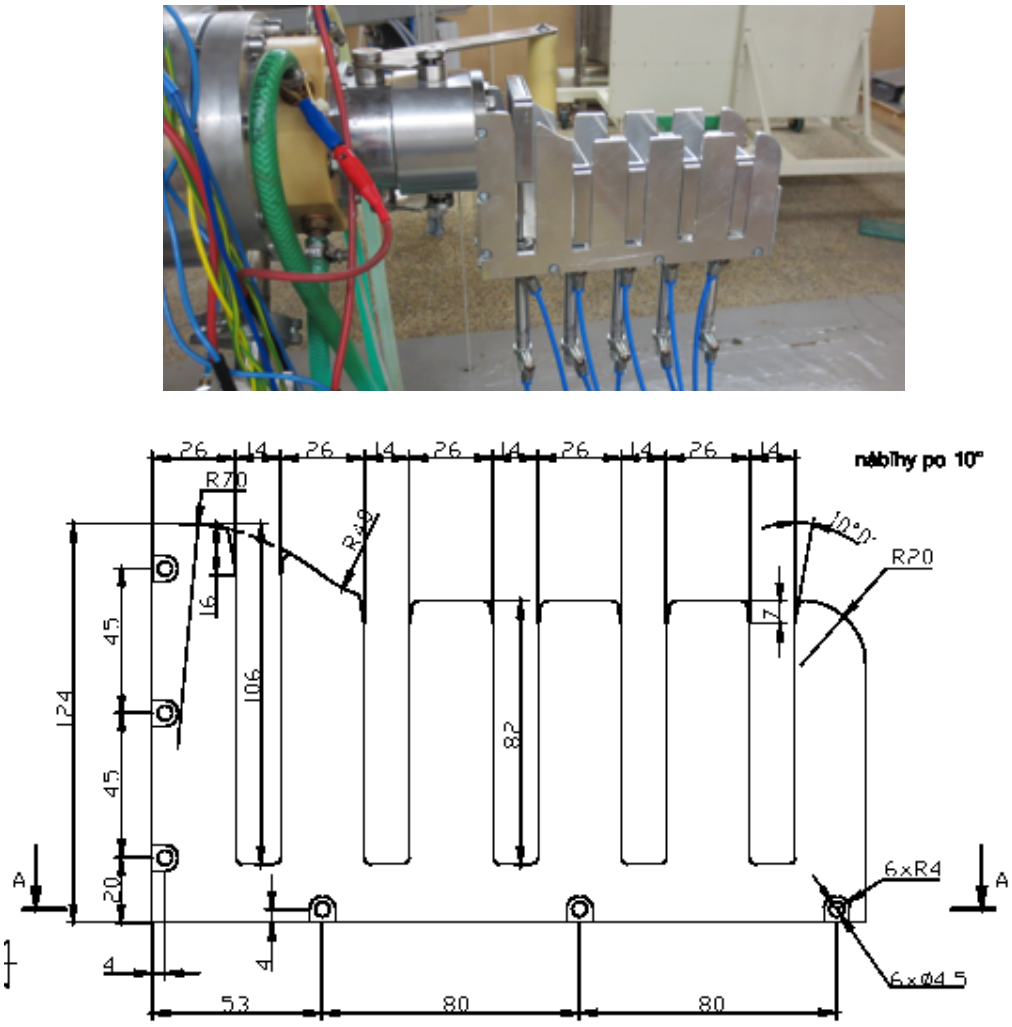

Figure 2.5: Top: The energy degrader mounted at the end of the cyclotron beam line from the negative mode. Taken from [27]. Bottom: Technical drawing of the energy degrader. All dimensions are in millimeters.

2.3 Ionization Chamber 30010 PTW Freiburg

The ionization chamber is a simple radiation gas-filled detector. The basic principle of the ionization chamber is to collect all charge generated by the radiation in the working gas of the chamber by application of an electric field. The generated charge is in the form of free electrons and ions. In the electric field they move to the electrodes of the opposite polarity, called the anode and the cathode. This creates an ionization current that can be measured by a sensitive ammeter. The ionization chamber works in the regime of proportionality, when the collected charge is proportional to the obtained radiation dose. A schema how the ionization chamber operates is shown in Figure 2.6.

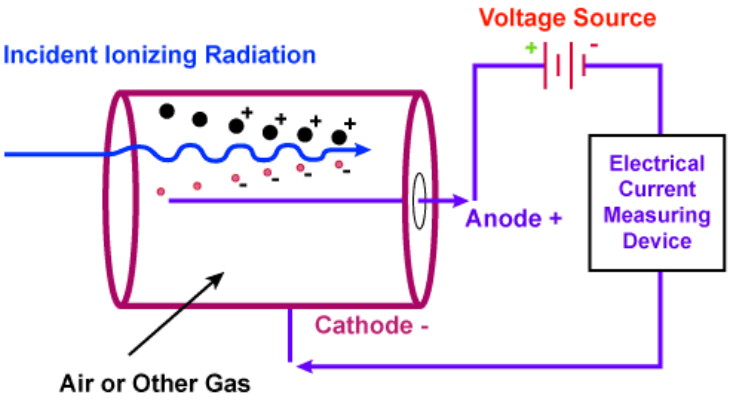

Figure 2.6: Schematic diagram the ionization chamber, showing basic parts and drift of ions and electrons. Taken from [28].

In our measurement we used the ionization chamber PTW 30010 [6]. The geometry of this chamber is cylindrical with a coaxial arrangement of internal aluminum wire, a graphite wall electrode and a protective film Polymethyl methacrylate (PMMA). The working gas of the chamber is the air at atmospheric pressure. The mean energy necessary to create one electron-ion pair thus equals 34 eV [8, 13]. The vented sensitive volume of the ionization chamber is 0.6 cm^3. Figure 2.7 shows a photography of the ionization chamber PTW 30010 together with its technical drawing.

The chamber is operated by means of the UNIDOS E, a microprocessor controlled universal dosimeter [29]. The UNIDOS E device allows to set voltage on the ionization chamber and reads the ionization current. The voltage set on the chamber can be changed from 0 to 400 V with 50 V increments. The nominal working voltage of the chamber is 400 V. The collection time of ions at the nominal voltage is 0.14 ms [30].

Within the allowed voltage range (50 to 400 V) we measured the current-

voltage characteristics of the ionization chamber for several proton beam intensities, see Table A.2. The data suggest that for the voltages between 50 and 400 V the measured ionization current is largely independent of the voltage. The chamber thus works in the regime where all generated charges participate in the ionization current and the recombination between them is minimal. The manufacturer guarantees that the chamber should provide linear response in a broad range of fluxes [30].

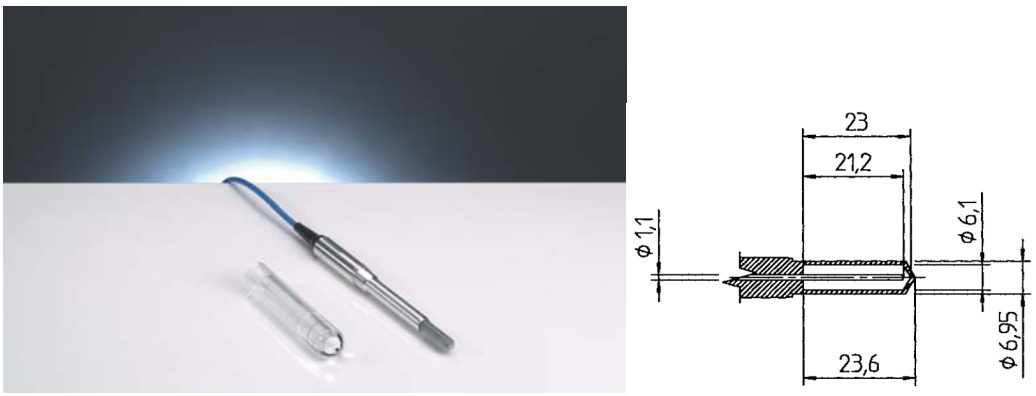

Figure 2.7: Left: Ionization chamber 30010 PTW Freiburg. Right: Technical drawing of the chamber. All dimensions are in millimeters. The wall of the PMMA cylinder is 0.335 mm thick. The wall of the graphite cylinder has a thickness of 0.09 mm. The diameter of the central aluminum electrode is 1.1 mm. Taken from [30].

2.4 Timepix

Timepix [31] is a planar silicone pixel detector derived from the Medipix2 development by an international collaboration hosted by CERN. The Timepix chip falls into the category of hybrid detectors, i.e., detector with a sensitive semiconductor layer bonded on to an electronic chip. A working scheme of a hybrid pixel detector is shown in Figure 2.8.

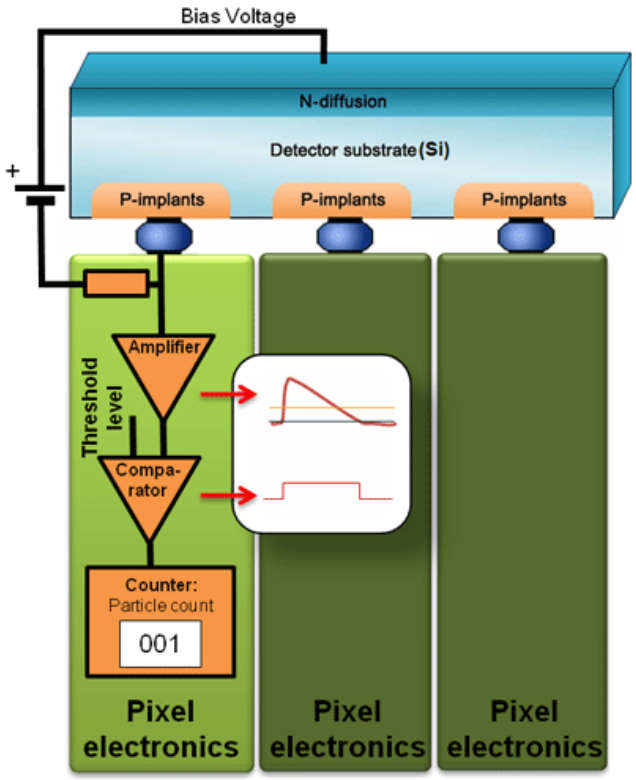

Figure 2.8: Working scheme of the electronics inside of the Timepix detector. The charge is collected from detector the substrate and the signal is amplified in an amplifier, subsequently the signal is going through a comparator, where after exceeding a threshold signals are converted to a rectangular pulse. The length of the rectangle represents time over threshold. Taken from [32].

A charged particle passing through the semiconductor layer of the chip induces an electron/hole cloud. The charge is subsequently collected in surrounding pixels. The signal is processed in every single pixel individually. First, it undergoes amplification and then the signal amplitude is compared with a pre-set discrimination level (energy threshold). If the signal amplitude is above the discrimination level the counter in the appropriate pixel is increased by 1, this simple counting mode is similar to the mode used by Medipix2.

The Timepix chip has two additional operation modes to the simple counter mode. The first one is the *Time-over-Threshold* mode which counts in each pixel the number of clocks for which the pulse remains above the discrimination level. This number is proportional to the energy that was deposited in a given pixel. The relation between the time over threshold (TOT) and the energy E deposited in the pixel can be expressed as

$$TOT = a \cdot E + b - \frac{c}{E - t} \tag{2.4}$$

where a, b, c and t are calibration parameters and E is the energy in keV. To get E as a function of TOT we need to invert the equation. This leads to a quadratic equation that can be easily solved. Finally we arrive to

$$E = \frac{TOT + ta - b + \sqrt{(TOT - ta - b)^2 + 4ac}}{2a}. \tag{2.5}$$

The second additional operation mode of the Timepix chip is the *Time-of-arrival* mode. The counter in this mode records the time between the trigger time and the registration of the leading edge of a pulse which exceeds the discrimination level. This mode can be used in applications for Time of Flight measurements [33].

Figure 2.9 shows the Timepix detector used in our measurement. The chip has 256×256 pixels. Each of them is a square having a side of $55\,\mu$m. The total sensitive area of the chip is $1.982\,\mathrm{cm}^2$. The semiconductor layer of our chip is made of silicon.

Figure 2.9: Timepix chip used in our measurements. [27]

We have cross-checked the energy calibration of our Timepix detector using gamma lines from several radioactive sources. In Figure 2.10 we show the results obtained with the isotope ^{203}Hg which emits just one gamma line with an energy of 0.279 MeV [34]. The left-hand side panel presents typical clusters emerging from the energy depositions left by the 0.279 MeV gamma photons in the Timepix chip. The right hand side panel shows the energy spectrum of these depositions. The line 0.279 MeV is clearly visible. Based on our measurement we conclude that the energy calibration of our Timepix detector is correct.

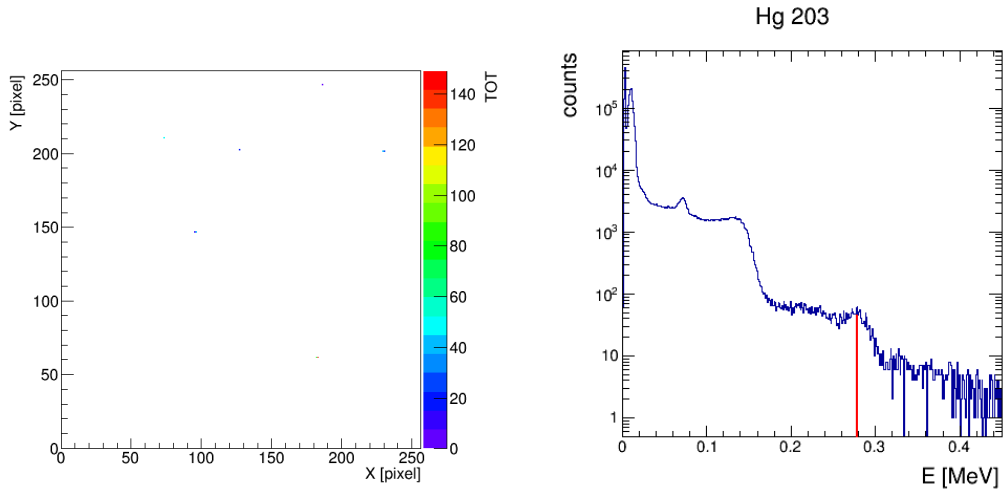

Figure 2.10: Left: Clusters emerging from the energy depositions induced by the 0.279 MeV gamma photons in the Timepix chip. Right: Energy spectrum of the gamma radiation emitted by the ^{203}Hg isotope measured by the Timepix. The red line marks the energy 0.279 MeV.

2.5 Setup

A schema of the setup used for our measurement is shown in Figure 2.11 and Figure 2.12. As it is indicated, protons from the negative mode of the cyclotron pass through the beam pipe exit window, the degrader, and 130 cm of air before they hit the ionization chamber and the Timepix. Both detectors were placed on a remotely controlled micrometric table MCL–3 from the LANG company [35]. The micrometric table can move independently in vertical and horizontal direction. Besides the sensitive chip, the rest of the Timepix detector is fully shielded by a 8 mm thick aluminum plate. The ionization chamber is fixed horizontally 1.9 cm below the center of the Timepix chip.

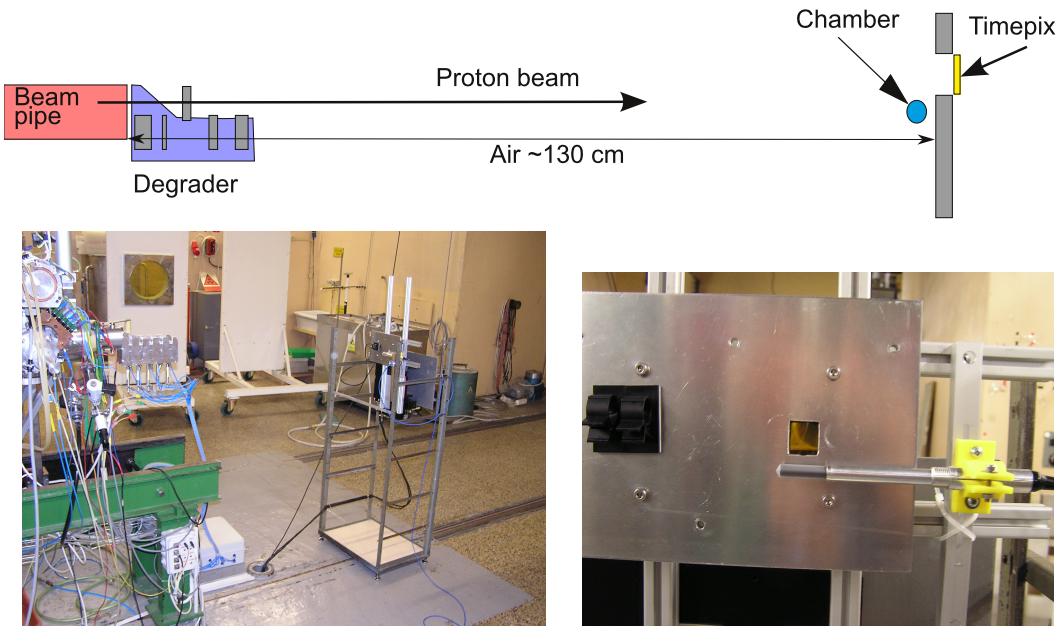

Figure 2.11: Top: Basic scheme of the setup used for the ionization chamber cross calibration and beam profile measurement. Bottom left: Experimental setup prepared for measurement with degrader mounted to exit of negative mode beam pipe and detectors placed on the micrometric table [27]. Bottom right: Detail of detectors placement on the micrometric table. During the beam profile scan the x axis is parallel with the ionization chamber axis and the y axis is perpendicular [27].

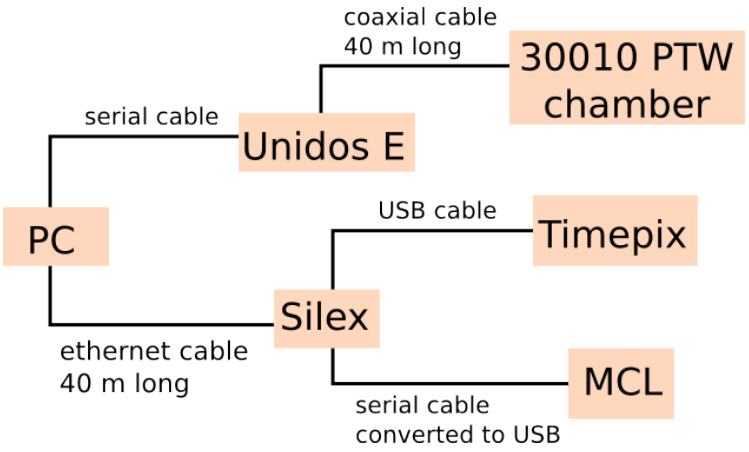

Figure 2.12: Scheme of the cable network used in the measurement.

Chapter 3

Analysis of Experiment

3.1 Measurement Conditions

The kinetic energy of the proton beam was 34.844 MeV on November 24 and 34.858 MeV on November 25. The duty factor was set to 5 %. The measurement was done without the beam focusation [36].

The working gas of our ionization chamber is the air. The response of the ionization chamber to incoming protons thus depends on the conditions that were in the cyclotron hall during the measurement, i.e. on November 24 and 25 in 2015. The pressure, temperature and relative humidity of the air as a function of time were monitored using the commercial DT-174B Datalogger [37]. The corresponding trends are shown in Figures 3.1, 3.2 and 3.3. Based on this data we conclude that the conditions throughout the measurement were stable. The average values of air pressure, temperature and relative humidity are given in Table 3.1. The quoted uncertainties in Table 3.1 give the statistical error of the mean value and the systematic uncertainty of the precision of the DT-174B Datalogger guaranteed by the manufacturer [37], respectively.

	24. 11. 2015, 13:58-17:34	25. 11. 2015, 9:22-14:15
Temperature [°C]	$25.13 \pm 0.03 \pm 1$	$25.417 \pm 0.008 \pm 1$
Pressure [hPa]	$1009.88 \pm 0.04 \pm 0.25$	$1010.54 \pm 0.02 \pm 0.25$
Relative humidity [%]	$34.51 \pm 0.03 \pm 3.5$	$32.35 \pm 0.04 \pm 3.5$

Table 3.1: Mean values of temperature, pressure and relative humidity in the cyclotron hall. The quoted errors give statistical error of the mean and the accuracy of the DT-174B Datalogger declared by the manufacturer.

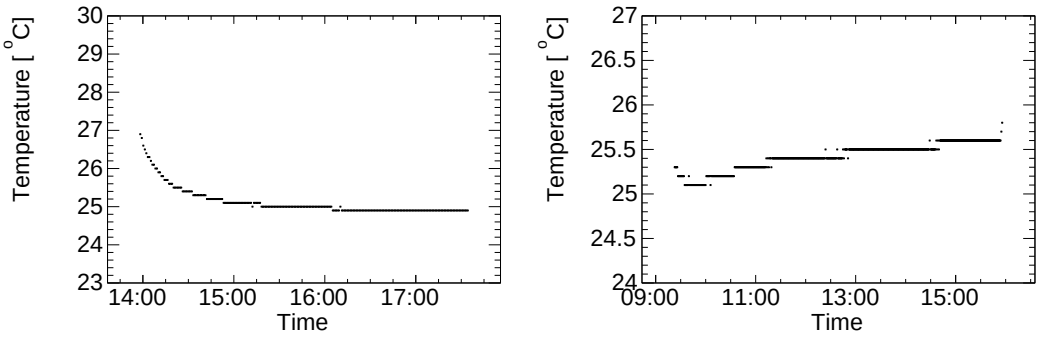

Figure 3.1: Air temperature in the cyclotron hall as a function of time. Left: 24. 11. 2015, Right: 25. 11. 2015

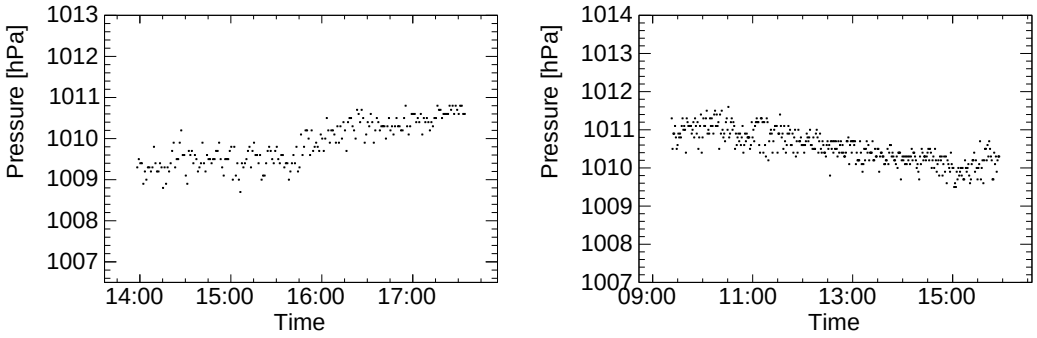

Figure 3.2: Air pressure in the cyclotron hall as a function of time. Left: 24. 11. 2015, Right: 25. 11. 2015

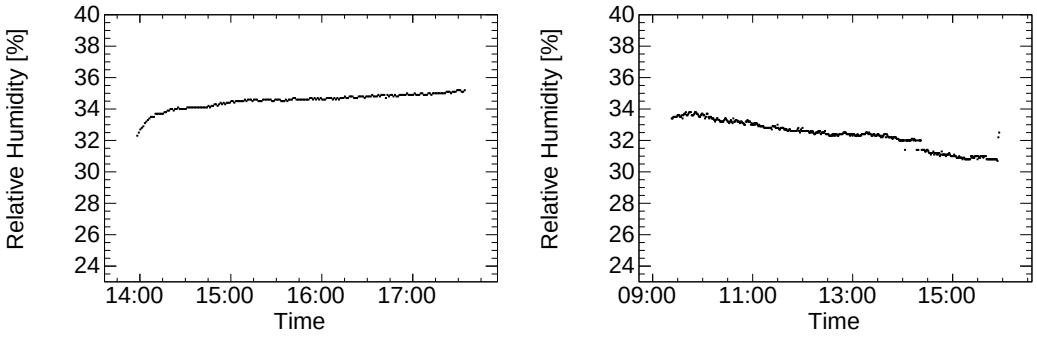

Figure 3.3: Relative humidity of air in the cyclotron hall as a function of time. Left: 24. 11. 2015, Right: 25. 11. 2015

3.2 Beam Profile Measurement

The transverse profile of the beam was measured on 24. 11. 2015 from 15:59 to 17:15 using the ionization chamber and the Timepix detector. We used 8 different configurations of the aluminum plates in the degrader and for each of them we scanned the beam in x and y with the ionization chamber. The scan went always through the point where the beam intensity reached its maximum. The scan was done in steps of 1 cm.

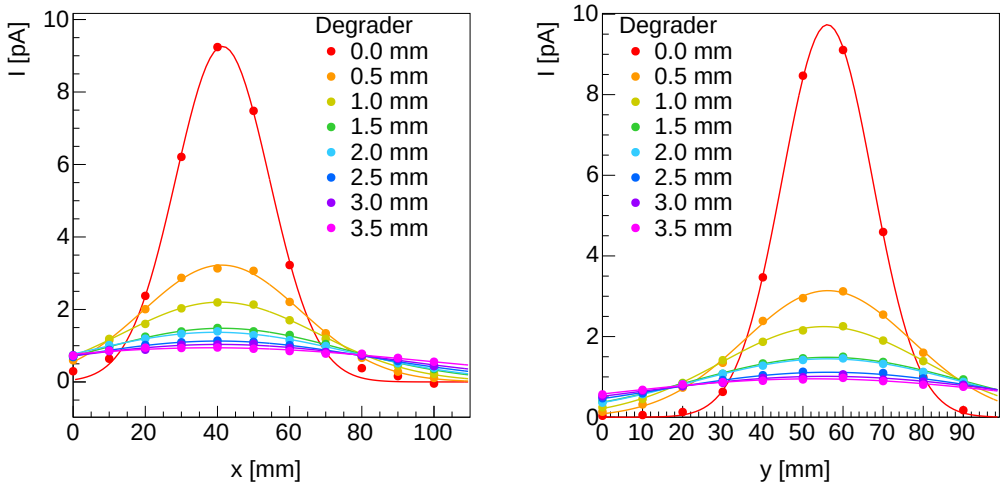

Figure 3.4: Transverse beam profiles measured with the ionization chamber along the x direction (left) and the y direction (right) for 8 different configurations of aluminum plates in the degrader. The total thickness of aluminum plates which were in the beam is given in the legend. The data points are shown without error bars and they are fitted with Gaussian functions.

The measured profiles are shown in Figure 3.4 They were fit with a Gaussian function,

$$I(x) = A \cdot \exp\left(-\frac{(\xi - \mu_\xi)^2}{2\sigma_\xi^2}\right), \tag{3.1}$$

where A is the amplitude, σ_ξ corresponds to the beam width, μ_ξ denotes the position of the mean, and ξ is x or y according to along which coordinate was the scan performed. The fit parameters are plotted as a function of the total thickness of the degrader plates inserted to the beam in Figure 3.5 and Figure 3.6. We see that as the material budget increases the beam profile gets wider. Degrader plates do not change the position of beam center. The multiple scattering thus helps to make the beam profile spatially more homogeneous at the irradiation spot, cf. section 1.2. In addition, the right hand side plot in

Figure 3.6 proves that the beam intensity gets reduced when more material is inserted to the beam.

An independent measurement of the beam width was obtained also from the distribution of proton clusters on the Timepix chip, see Figure 3.8. Because the size of the Timepix chip is small ($\sim$2 cm^2), the width of the beam profile could be measured accurately enough only in the case when there was no plate in the degrader, see Figure 3.7. The Gaussian widths σ_x and σ_y obtained from the fit of Timepix data are the same within errors and are comparable with the values measured by the chamber, see Figure 3.5. This was very surprising result as it was expected that the asymmetric profile of the chamber (2.1 cm$\times$0.6 cm) would cause significantly larger smearing along the longer axis. Nevertheless, a simple mathematical argument why the chamber yet provides quite accurate information about the beam profile is presented in the next chapter.

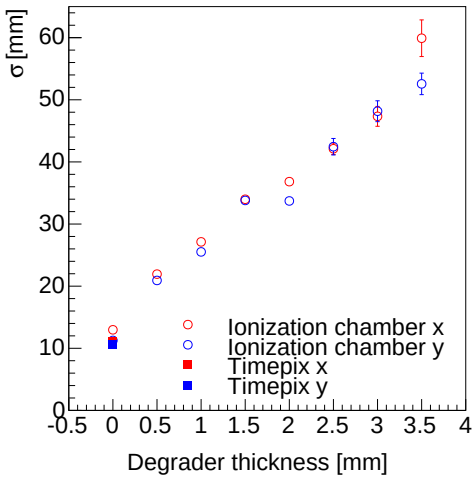

Figure 3.5: Beam width in the x direction (red circles) and the y direction (blue circles) measured with the ionization chamber for 8 different degrader configurations. The red (blue) square marker shows the beam width along the x (y) direction extracted from the Timepix detector when there was no aluminum plate placed in the beam.

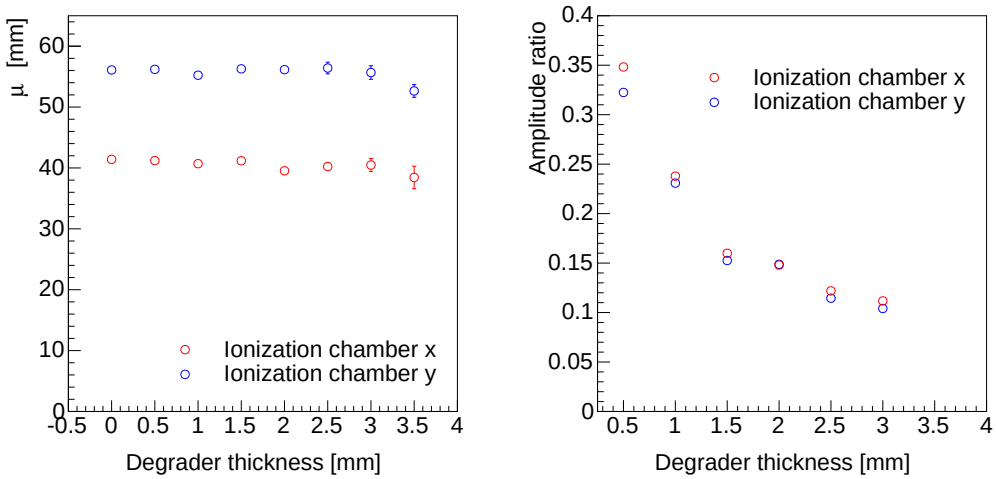

Figure 3.6: Left: x and y coordinates of the beam center obtained from the Gaussian fits shown in Figure 3.5. The data are plotted as a function of the total thickness of the aluminum plates placed in the beam. Right: The relative size of the beam amplitude as a function of the total thickness of the aluminum plates inserted to the beam. The amplitudes are given relative to the case when there was no degrader plate placed in the beam. The data from the scan along x and y direction are shown separately.

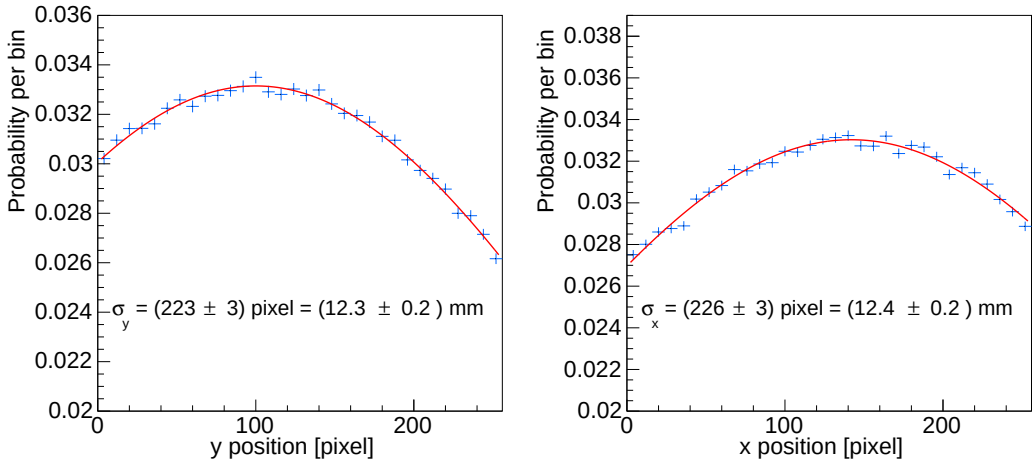

Figure 3.7: Distribution of proton cluster centroids on the Timepix chip in the x (left) and y (right) direction. The data are fitted with a Gaussian function. The known size of a Timepix pixel (55 μm) enables to convert the extracted Gaussian width from pixels to millimeters.

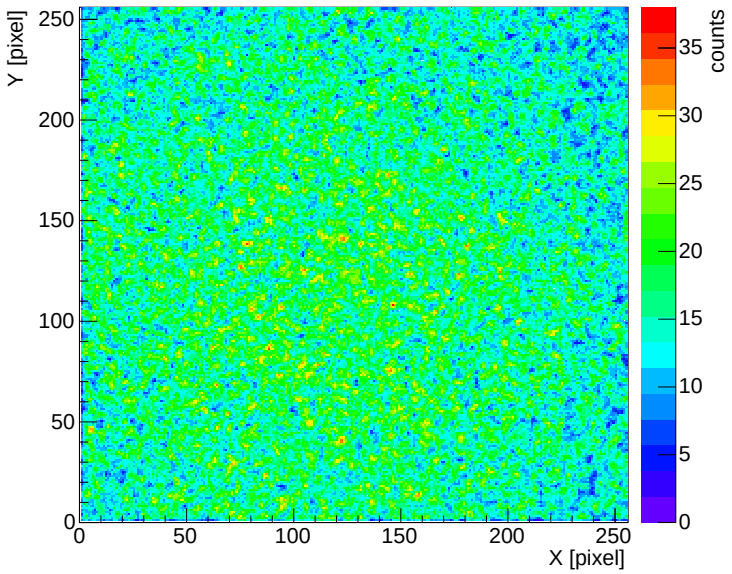

Figure 3.8: The number of entries in individual Timepix pixels. The z axis shows how many times given pixel was a part of a big cluster (area ≥ 6).

3.3 Toy Model Calculation of the Ionization Current in the Chamber

In this paragraph we present a simple back-of-the-envelop calculation which estimates to what extent the finite dimensions and asymmetric profile of the ionization chamber influence the measured transverse profile of the proton beam.

Lets assume that the profile of the proton beam follows a two dimensional symmetrical Gaussian function

$$f(x,y) \approx \exp\left(-\frac{x^2+y^2}{2\sigma^2}\right) \tag{3.2}$$

where x and y are Cartesian coordinates and σ denotes the width of the proton beam.

Further we will assume that the ionization chamber has a simple cylindrical geometry as shown in Figure 3.9. Yet another assumption to be made is that all protons traversing the chamber follow straight parallel lines and that the generated ionization current by one proton is proportional to the traversed path length in the sensitive volume of the chamber. The long axis of the ionization chamber is parallel with the x axis. The center of the chamber is located at the point (x_0, y_0). The proton beam is oriented along the z axis.

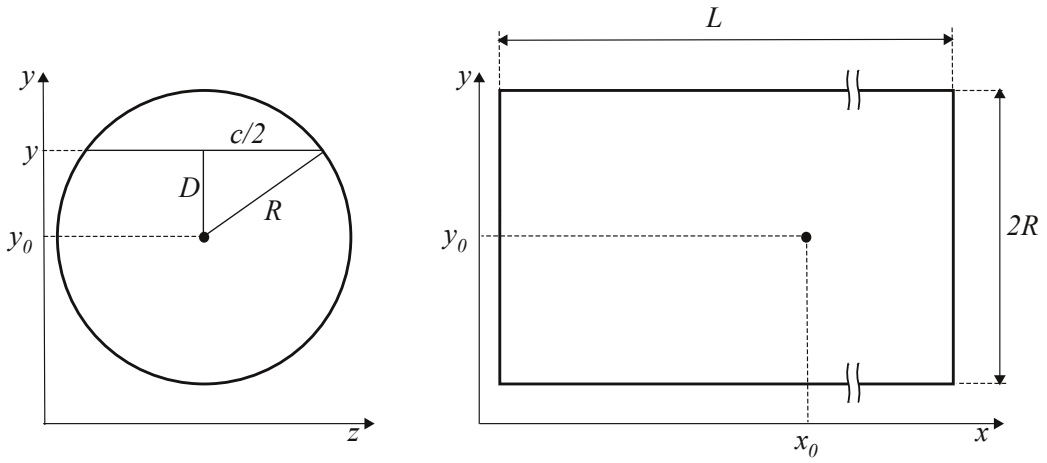

Figure 3.9: Left: cross section of the chamber in the yz plane. Right: cross section of the chamber in the xy plane.

Proton moving along the line with fixed x and y coordinates will traverse in the sensitive volume of the ionization chamber a path length c, which can

be calculated using the Pythagorean theorem,

$$\frac{c}{2} = \sqrt{R^2 - D^2} = \sqrt{R^2 - (y - y_0)^2}, \tag{3.3}$$

where R is the radius of the ionization chamber, D is the transverse distance of proton trajectory from the chamber center which can be expressed in terms of the ionization chamber position coordinate y_0 and the proton y coordinate.

Following from (3.3) the measured current can be expressed by the integral

$$I(x_0, y_0) \propto \int_{x_0 - \frac{L}{2}}^{x_0 + \frac{L}{2}} \int_{y_0 - R}^{y_0 + R} e^{-\frac{x^2 + y^2}{2 \cdot \sigma^2}} \cdot 2 \cdot \sqrt{R^2 - (y - y_0)^2} \mathrm{d}x \, \mathrm{d}y, \tag{3.4}$$

where we integrate the path length of all protons traversing the chamber and give to each contribution a weight proportional to the assumed beam profile (3.2). The upper and lower integration limits correspond to the acceptance of the chamber at given position (x_0, y_0). The length of the ionization chamber is denoted L.

From (3.4) it follows that

$$I(x_0, y_0) \propto 2 \int_{x_0 - \frac{L}{2}}^{x_0 + \frac{L}{2}} e^{-\frac{x^2}{2 \cdot \sigma^2}} \int_{y_0 - R}^{y_0 + R} e^{-\frac{y^2}{2 \cdot \sigma^2}} \cdot \sqrt{R^2 - (y - y_0)^2} \, \mathrm{d}y = \tag{3.5}$$

$$= \sqrt{2\pi}\sigma \left[\operatorname{erf}\left(\frac{x_0 + \frac{L}{2}}{\sqrt{2}\sigma} \right) - \operatorname{erf}\left(\frac{x_0 - \frac{L}{2}}{\sqrt{2}\sigma} \right) \right] \cdot \int_{y_0 - R}^{y_0 + R} e^{-\frac{y^2}{2 \cdot \sigma^2}} \cdot \sqrt{R^2 - (y - y_0)^2} \, \mathrm{d}y \tag{3.6}$$

The integral in (3.6) does not have an analytic solution, therefore, it was solved numerically in ROOT. Namely, we calculated the current in the chamber in several positions along the y axis having the x_0 fixed at 0. Afterwords we fixed $y_0 = 0$ and repeated the same calculation along the x axis. The calculation was done for several beam widths in the range from 10 to 60 mm, see Figure 3.10. As can be seen from Figure 3.10, the finite dimensions of the chamber cause that the initially symmetric beam profile gets more smeared in the scan which proceeds along the long axis of the chamber. The Figure 3.10 also suggests that the difference between the measured beam profile in the x and y scan increases when the initial beam width gets narrow. In order to quantify this difference, the calculated beam profiles were fit with a one dimensional Gaussian function (3.1). The obtained difference between the initial beam width σ and the fitted width σ_{ch} is shown in Figure 3.11, where this difference is plotted as a function of the initial beam width. We see that the scan along the short axis should cause only a negligible broadening

($\approx 0.1\,\mathrm{mm}$) of the initial width. The scan along the long axis causes larger smearing. Nevertheless, even in the worst considered case the difference does not exceed 2 mm and for the usual beam profiles it stays around 0.5 mm which is perfectly acceptable for our measurements.

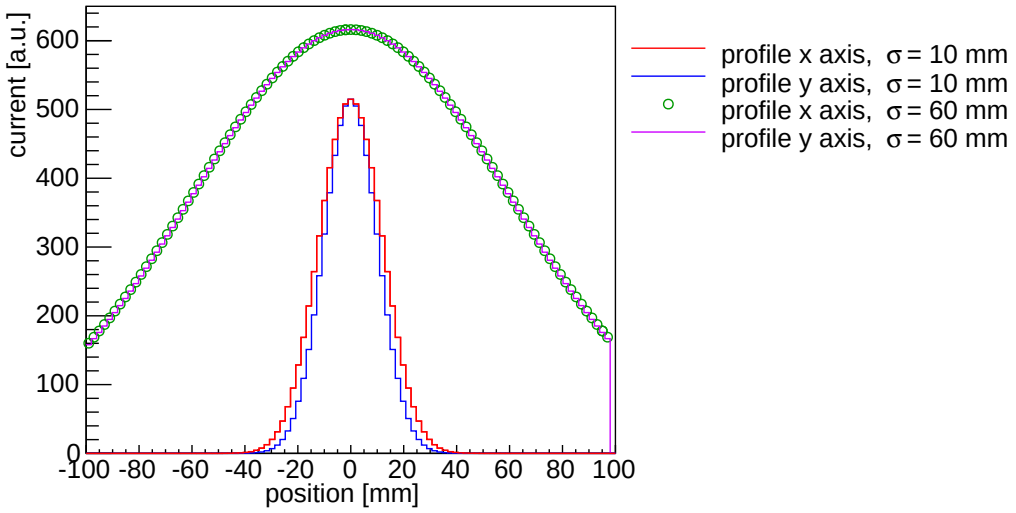

Figure 3.10: Ionization current in the chamber as a function of its position. The current is calculated from (3.6) for the case when the chamber was moving along y with x_0 being fixed at 0 (blue and purple distribution) and for the case when the chamber was moving along x with y_0 being fixed at 0 (red and green distribution). The initial beam width was set to 60 mm and 10 mm.

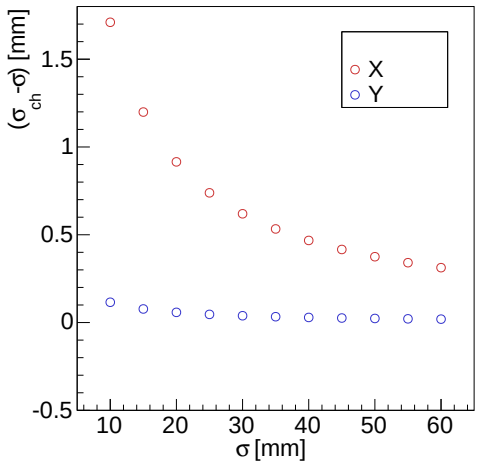

Figure 3.11: Difference between the beam profile width σ_{ch}, obtained from the fit of (3.6) by (3.1), and the initial beam profile width σ. The difference is shown as a function of σ. The red points (blue points) correspond to the scan along the long (short) axis of the chamber.

3.4 Data Taking

In this section, we describe how was the ionization chamber current correlated with the number of protons detected by the Timepix. Throughout our measurement we used the following Timepix settings: bias voltage 100 V, positive polarity and $I_{krum} = 1$. The ionization chamber was operated at the standard voltage 400 V.

The ionization chamber was placed to the point with the highest beam intensity and we measured the ionization current for ca. one minute. Afterwards we moved the Timepix to the beam center, initiated data acquisition, and we continued to measure the ionization chamber current now in the position at the tail of the beam profile. We carried out this measurement for nine different configurations of the plates in the degrader and several beam intensities.

An example of the ionization chamber current monitoring is presented in Figure 3.12. It shows a short time sequence during which the ionization chamber was replaced by the Timepix at the beam center. The Timepix measured 1000 frames and each of them lasted 1 ms. Note that the sampling of the Timepix frames was completely random in time. It was driven by the speed of data transfer to the memory of our computer.

To estimate the proton flux going through the sensitive area of the Timepix we used a ROOT based graphic user interface (GUI) developed by the Czech ALICE group. The GUI enables to do event by event visualization of Timepix

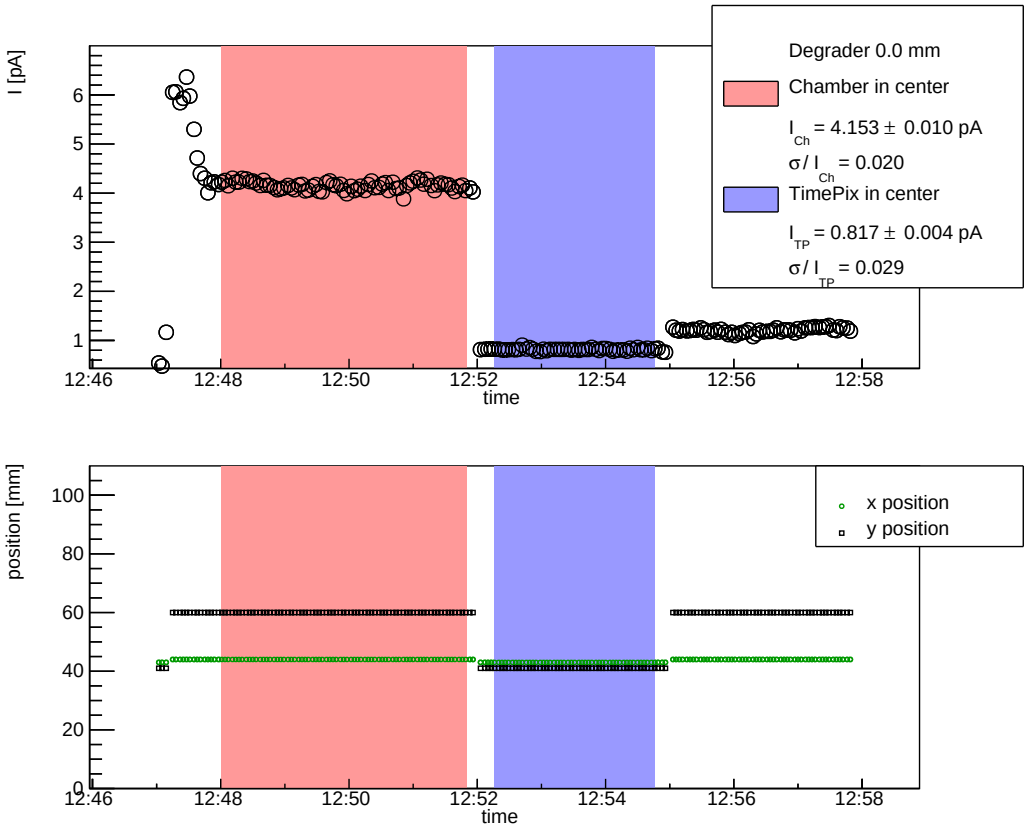

Figure 3.12: Top panel: Current measured by the ionization chamber as a function of time. The red and blue boxes highlight the time windows when the ionization chamber and the Timepix were at the beam center, respectively. The legend quotes the corresponding mean values of the ionization chamber current. Further we quote the ratio of the standard deviation to the mean value. This ratio provides information about the magnitude of beam intensity fluctuations in time. Bottom panel: Corresponding positions of the micrometric table in time. The measurement was carried out on November 24 in 2014. During this measurement there was no degrader plate in the beam.

frames and is equipped with a cluster search algorithm which allows to count protons. By a cluster we mean a set of adjacent pixels that have nonzero TOT and form a connected group, see Figure 3.13. The clusters induced by protons can be easily identified since the proton creates a large energy deposits ($\sim$MeV) in the Timepix chip. The released charge then tends to diffuse to the neighboring pixels creating thus clusters with relatively large area. However, besides the single proton clusters and merged proton clusters Timepix frames contain also another kind of cluster thus clusters which can be characterized with by a small cluster area and relatively large TOT. Actually, the TOT of

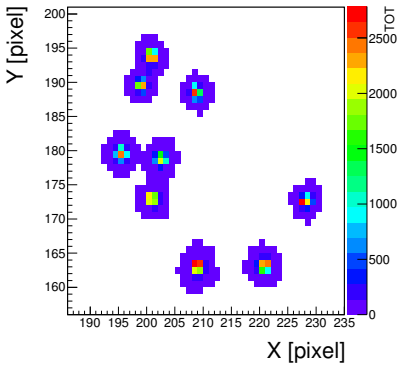

Figure 3.13: The proton clusters detected by the Timepix. The GUI would find on the figure 6 clusters.

these "small clusters" was usually similar or even larger when compared to the mean proton response; compare the TOT on the$z$ axis of the left and right hand side panel in Figure 3.14. The exact nature of these "small clusters" was not clear. Some of small clusters can originate from photons. However, photon signal have smaller TOT $\sim$140, see right hand side of Figure 2.10. The other possible sources of this signal could be e.g. incomplete readout of proton energy deposit, neutrons or some kind of electronic noise.

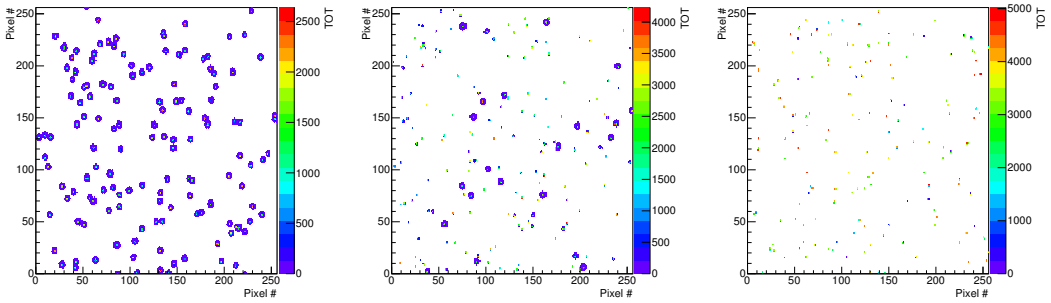

Figure 3.14: Types of frames recorded by the Timepix. Left: Frame contains only proton clusters. Center: Frame contains proton and small clusters. Left: Frame contains only small clusters.

Most of the small clusters have area less than 5 pixels see Figure 3.15. If we take that as a definition of what a small cluster is it is possible to make a statistics how often different kinds of clusters appear in frames. We have found out that $\approx 3\,\%$ of frames contain just the proton clusters, $\approx 22\,\%$ of frames have a mixture of the small and the proton clusters, $\approx 20\,\%$ of frames contain just the small clusters and $\approx 55\,\%$ of frames are empty, see Figure 3.14.

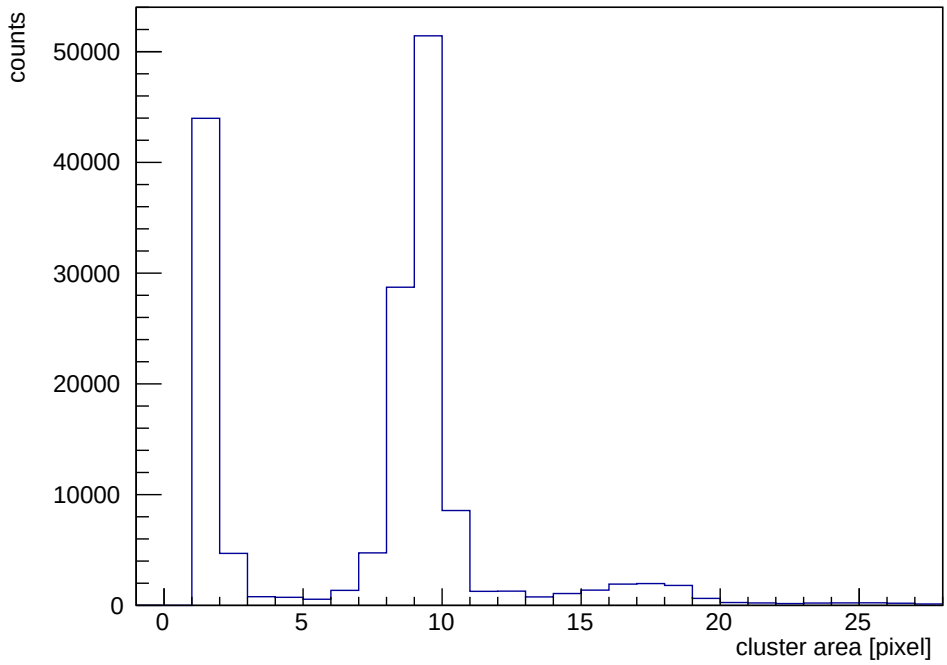

Figure 3.15: Cluster area distribution. The small clusters form the pronounced peak on the left. The clusters created by a single proton hit contribute to the peak around 10. The clusters resulting from two merged nearby proton hits form a peak around 17.

Looking at the spatial distribution of the small and proton clusters across the Timepix chip we have revealed that the small clusters follow the same spatial distribution as the protons. This is illustrated in Figure 3.16, where we compare the distribution of pixels belonging to the small and the proton clusters on the Timepix chip that was fully exposed to the proton beam and on the chip that was partially covered by a $\sim$8 mm thick aluminum plate, that stops the protons completely.

A clear evidence that the small clusters are just an electronic feature indigenous to the Timepix chip was, however, obtained in an experiment when we have measured how the number of the proton and the small clusters changes in time. In this experiment we have read the starting edge of the 150 Hz cyclotron filling pulse and afterwards we triggered the Timepix data acquisition using a well defined value of time delay, see Figure 3.17. In Figure 3.18 we see the number of clusters as a function of this delay. While the proton clusters appear only during the $\sim 333\,\mu$s time window (corresponding exactly to the 5% cyclotron duty factor), the small clusters tend to create a double hump struc-

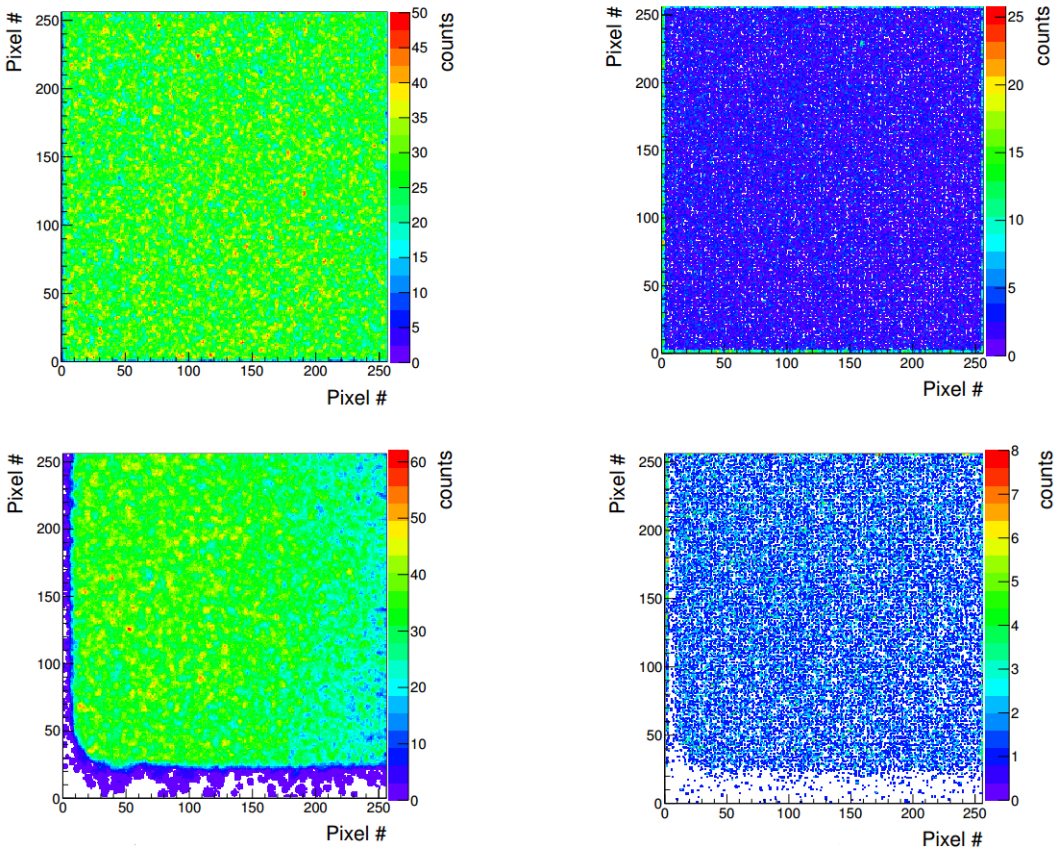

Figure 3.16: The number of entries in individual Timepix pixels. Plots show how many times a given pixel was a part of the proton cluster (left column) or the small cluster (right column). The Timepix chip was either fully exposed to the proton beam (top row) or partially shielded with an aluminum plate (bottom row).

ture. Artificial pulses produced in the Timepix detector were earlier reported also in [38].

For further analysis it is important that the small clusters can be effectively removed by applying a cut on area size. Farther we ignore all pixels which have TOT>4800 and rows of pixels where the average TOT exceeds 2500. Remaining clusters with area $\geq$6 pixels were used to count protons. The number of protons in all frames was estimated by three methods:

- counting local maxima of energy deposition in clusters $\left(N^{Local}\right)$,
- dividing the total area of all proton clusters by the area of an average single proton cluster $\left(N^{Area}\right)$,

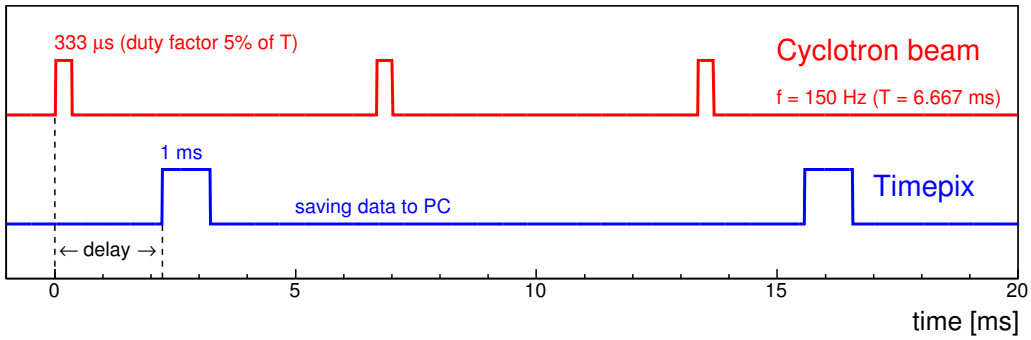

Figure 3.17: Time structure of the beam delivered by the cyclotron (red line). The blue line shows the course of data taking with the Timepix. The difference between the leading edge of the blue and the red lines gives the delay.

- dividing the total energy of all proton clusters by the energy of an average single proton cluster $\left(N^{Energy}\right)$.

The algorithm that is implemented in the GUI for the local maxima search first folds the raw two dimensional TOT map of fired pixels on the chip with a two dimensional Gaussian function. The local maxima are subsequently searched on this smeared image. This is a standard trick used in many pattern recognition techniques [39]. The clusters where we have found just one local maximum are called the *single proton clusters*. They represent a response of the Timepix chip to individual protons. Let us note that this method can provide somewhat biased results in the case when there is a significant probability that a large cluster will overlap with the small cluster or when the proton hits are too close.

The second method is more robust with respect to the case overlap, since the small clusters, since small clusters do not increase the area significantly. On the other hand this method will underestimate the total number of protons when there is a large probability that the large clusters overlap. The distributions of cluster area of all proton clusters and the single proton cluster are shown in Figure 3.19.

The third method should not be sensitive to overlaps of the large clusters. On the other hand it is sensitive to the cases when the small clusters and the large clusters merge. Then it will tend to enhance the number of protons. The distribution of cluster energy for all proton clusters and the single proton clusters are presented in Figure 3.20.

Since all three methods have their advantages and disadvantages, the re-

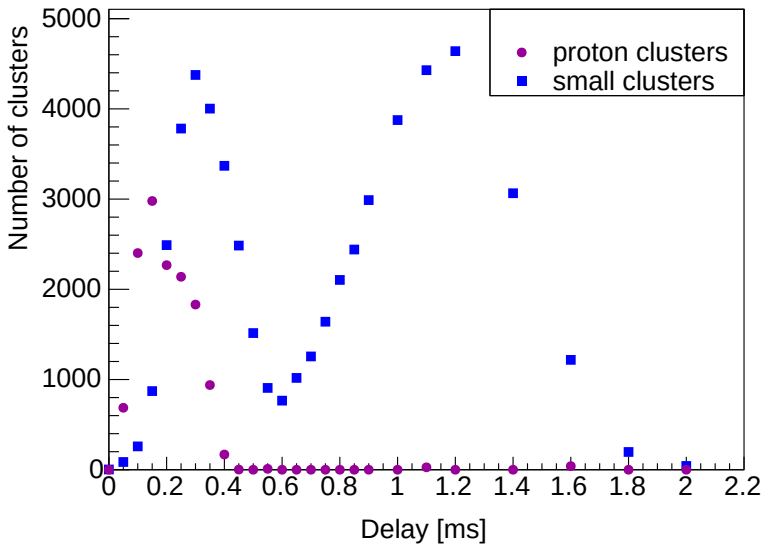

Figure 3.18: Top: The number of the proton clusters (violet circles) and the small clusters (blue squares) as a function of the delay between the cyclotron clock and the start time of the Timepix frame.

sulting number of protons was estimated by averaging their results

$$N_{protons} = \frac{N^{Local} + N^{Area} + N^{Energy}}{3}. \tag{3.7}$$

The uncertainty on $N_{protons}$ was considered to have a statistical and a systematic part. In general, the statistical uncertainty reflects the variability in results obtained by repeated independent measurements. Due to the lack of time we could measure each data point for given beam intensity and degrader configuration just once. Unfortunately in our case it is also not a priory clear whether the statistical uncertainty should have the usual Poissonian nature. Note that beam intensity fluctuations have origin partly in the processes that take place in the cyclotron. As each Timepix measurement comprise 1000 frames each lasting 1 ms the measured number of protons was affected by the beam fluctuations happening on the time scale of order of 1 s. The magnitude of these fluctuations was assessed based on the fluctuations in the current measured by the ionization chamber during the time when the Timepix was at the beam center. The corresponding time period is highlighted by the blue color box in Figure 3.12. We assume that the relative size of fluctuations across the beam profile is the same. The statistical uncertainty on $N_{protons}$ was estimated to be

$$\sigma_{N_{protons}} = N_{protons}\frac{\sigma_{TP}}{I_{TP}}, \tag{3.8}$$

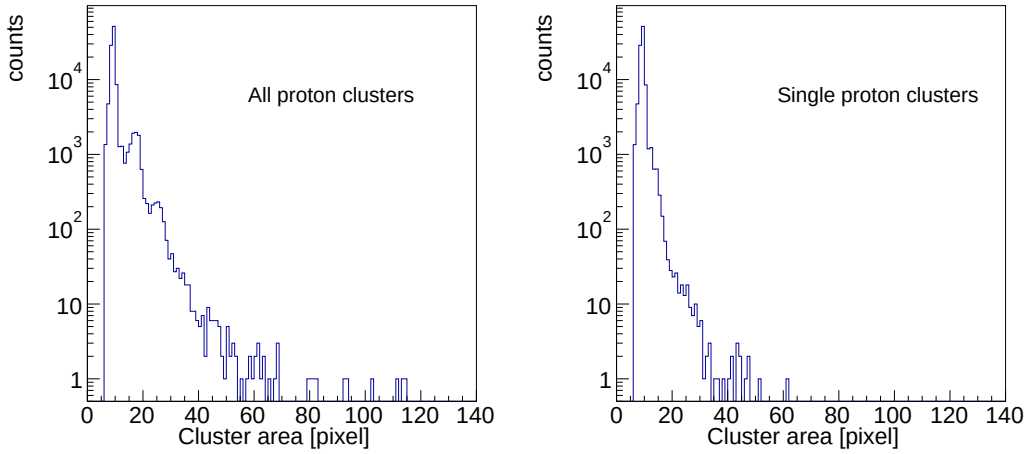

Figure 3.19: Left: The distribution of cluster area for all proton clusters with area $\geq$6. The local maxima appearing in the distribution correspond to the cases of one proton hit or several merged nearby proton hits. Right: The distribution of cluster area for the single proton clusters with area $\geq$6. Note that the peaks corresponding to merged nearby proton hits are largely suppressed. The distributions correspond to the case without any plates in the energy degrader.

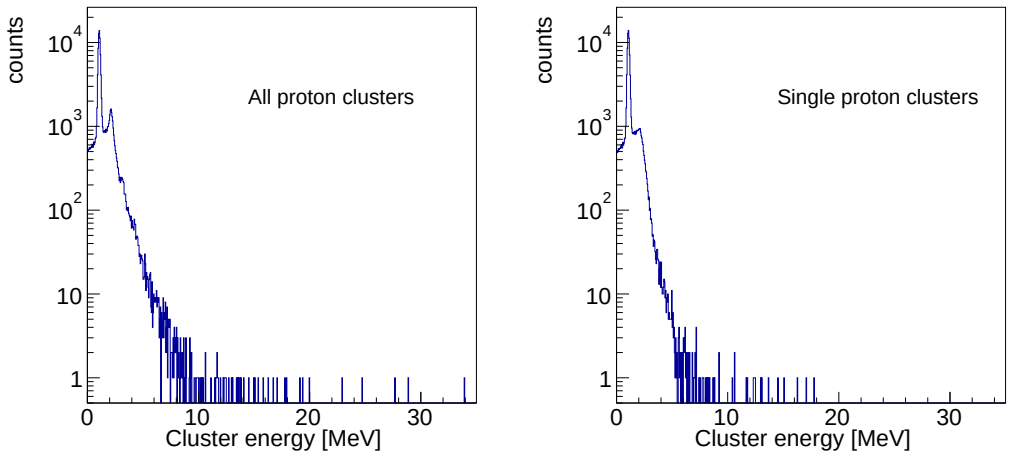

Figure 3.20: Left: The distribution of cluster energy for all proton clusters with area $\geq$6. The local maxima appearing in the distribution correspond to the cases of one proton hit or several merged nearby proton hits. Right: The distribution of cluster energy for the single proton clusters with area $\geq$6. The distributions correspond to the case without any plates in the energy degrader.

where I_{TP} and σ_{TP} are the mean current and its standard deviation measured by the chamber during the period when the Timepix was at the beam center.

A conservative estimate of the systematic uncertainty on $N_{protons}$ was obtained by taking the maximum positive and the maximum negative deviation of N_{Local}, N_{Area}, and N_{Energy} from $N_{protons}$.

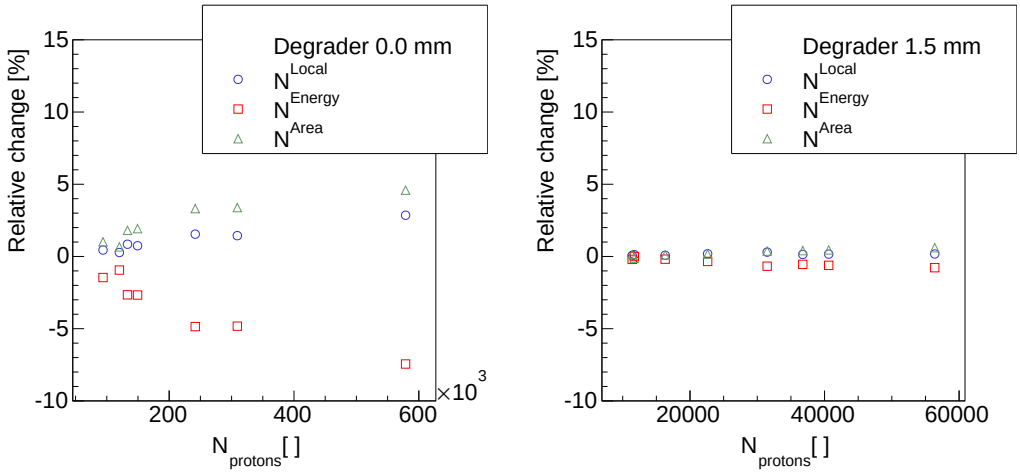

Figure 3.21: Relative change$(N^i, N_{protons})$=$\frac{N_{protons}-N^i}{N_{protons}}$ as a function of N_{proton} for $i \in \{Local, Area, Energy\}$. Left: Without degrader plates. Right: Total width of aluminum plates in the beam was 1.5 mm.

The proton flux equals

$$\phi = \frac{N_{protons}}{N_{frames} \cdot T_{frame} \cdot S} \ , \tag{3.9}$$

where N_{frames} is the number of frames, T_{frame} is duration of one Timepix frame and S is the area of the Timepix chip ($\sim 2\,\mathrm{cm}^2$).

3.5 Correlation Between the Proton Flux and the Ionization Chamber Current

Figure 3.22, Figure 3.23 and Figure 3.24 shows the proton flux calculated from (3.9) as a function of the mean current I_{ch} measured by the ionization chamber in the position at the beam center. The usual error propagation was used to convert the statistical and the systematic errors of N_{proton} to the uncertainties on ϕ. In Figure 3.22, Figure 3.23 and Figure 3.24 the statistical and the systematic uncertainties on the proton flux were added linearly. The correlation between ϕ and I_{ch} is manifestly linear as guaranteed by the manufacturer. The data were fitted with

$$\phi = k \cdot I_{ch} + b, \tag{3.10}$$

where k and b are parameters of the fit. The size of the b parameter for different degrader configurations is shown in Figure 3.25. In principle there is no reason why the b parameter should vary significantly when changing the configuration of plates in the degrader. The average b obtained from a fit of the data in Figure 3.25 by a zero order polynomial function is within error bars consistent with zero supporting the hypothesis of zero b. This indicates that the background level during our measurement was negligible. Therefore, from now on it will be assumed $b = 0$ and we will use a simpler fit form

$$\phi = k \cdot I_{ch}. \tag{3.11}$$

The resulting linear fits obtained for different degrader configurations are presented in Figure 3.26. The data show a clear trend, the more aluminum is placed to the beam the larger increase of I_{ch} with ϕ we get. This is consistent with the expectation that the stopping power of protons increases as their velocity decreases, cf. section 1.1.

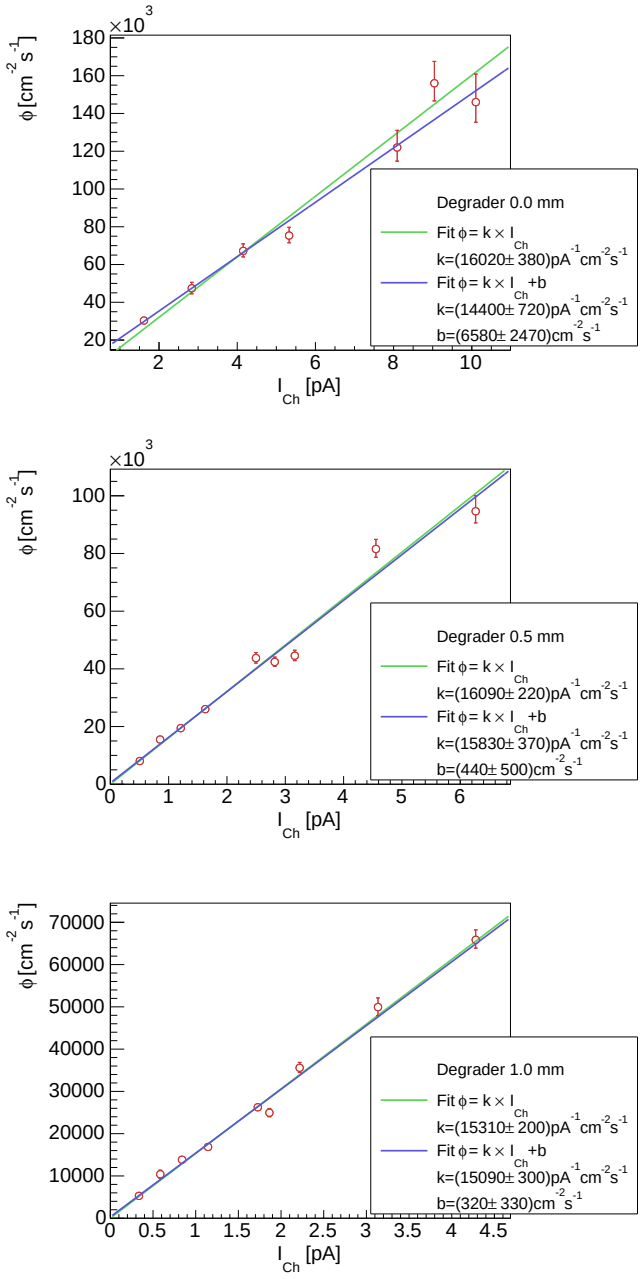

Figure 3.22: The measured ionization chamber current I_{ch} as a function of the proton flux ϕ determined from the analysis of Timepix frames. The data are fitted with two linear functions $\phi = k \cdot I_{ch} + b$ and $\phi = k \cdot I_{ch}$, where k and b are parameters of the fit. Thickness of the aluminum plates placed in the beam is 0.0 mm, 0.5 mm, 1.0 mm.

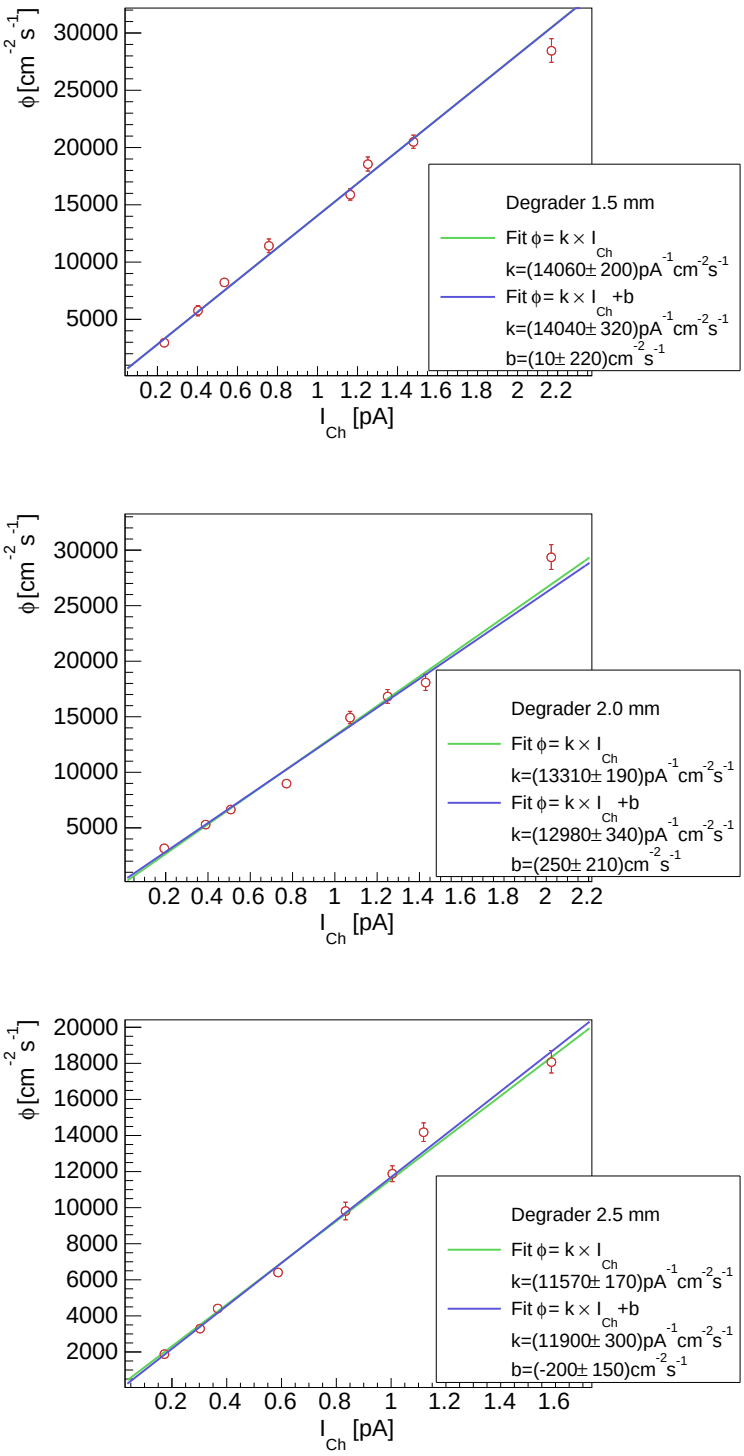

Figure 3.23: The same as Figure 3.22. Thickness of the aluminum plates placed in the beam is 1.5 mm, 2.0 mm, 2.5 mm.

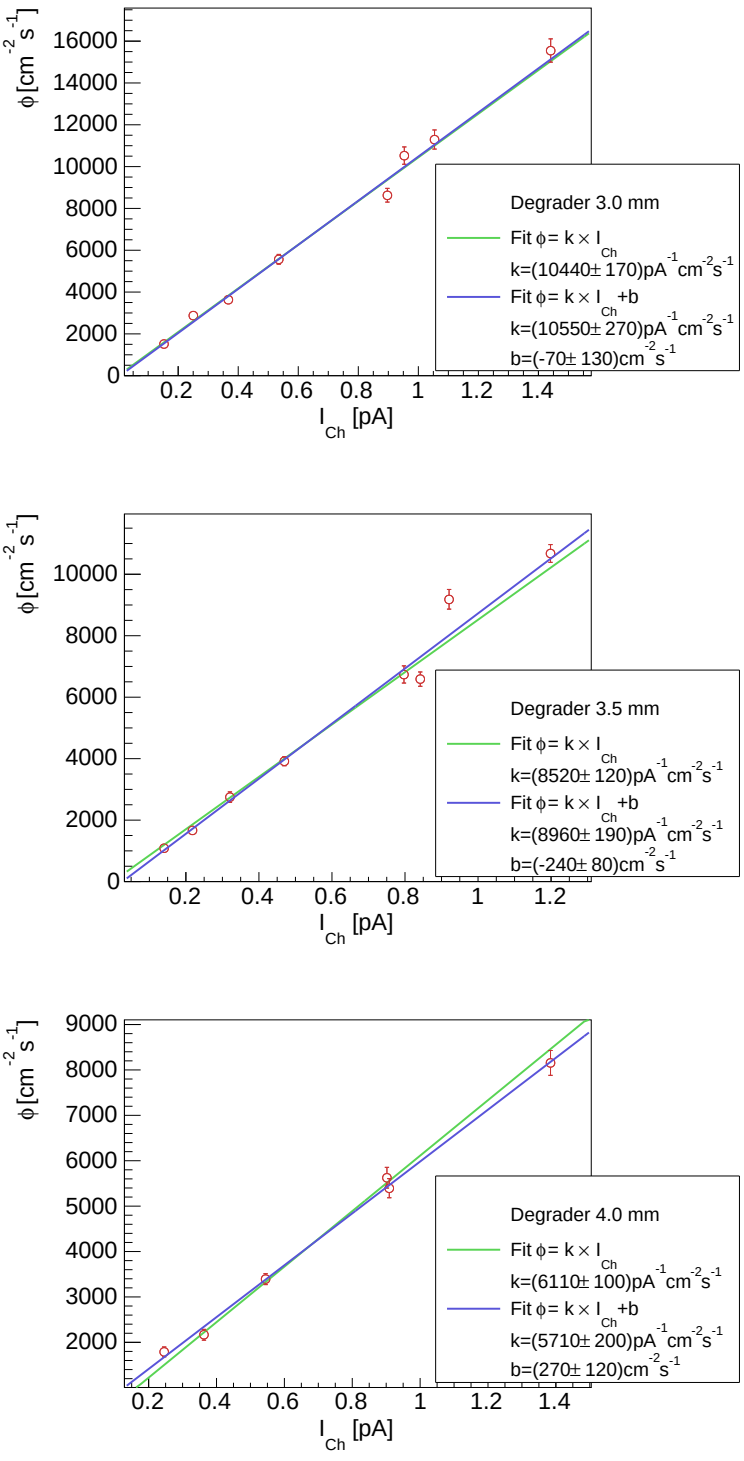

Figure 3.24: The same as Figure 3.22 . Thickness of the aluminum plates placed in the beam is 3.0 mm, 3.5 mm and 4.0 mm.

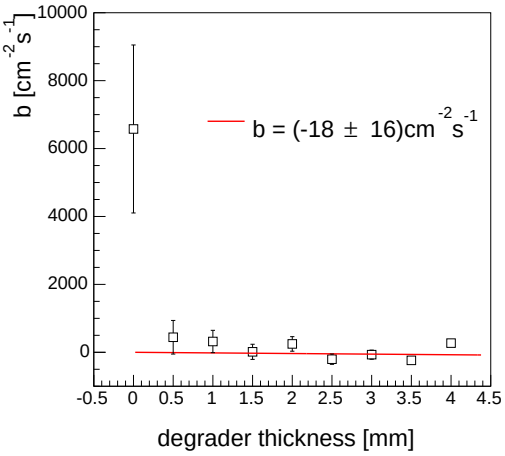

Figure 3.25: Size of the b parameter obtained for different degrader configurations. The data are fitted with a constant function.

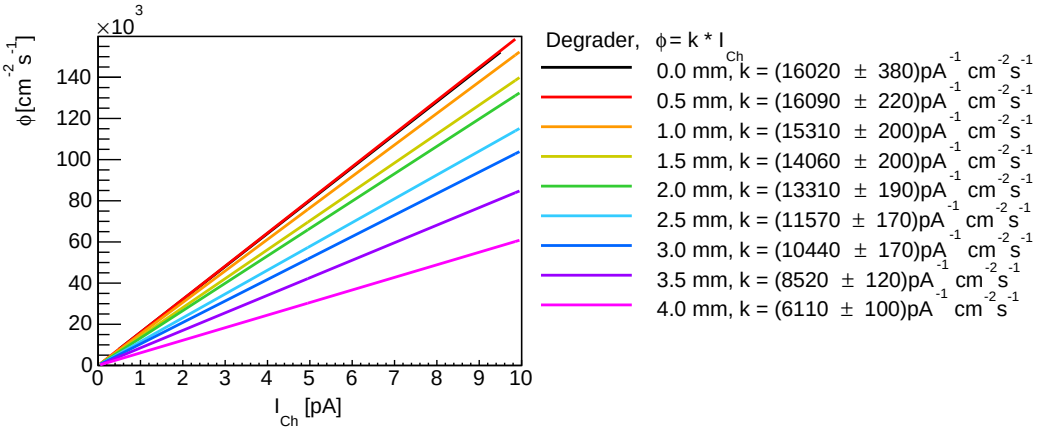

Figure 3.26: Fitted calibration curves for all degrader configurations

Chapter 4

Simulations

In this chapter we use the Geant4 and SRIM simulations to study

- how different parts of our experimental setup affect the proton beam parameters and
- how large energy depositions do the incoming protons leave in the detectors Timepix and ionization chamber.

The final goal of this chapter is to get the quantitative understanding of the obtained calibration curves in Figure 3.26 based on Geant4 simulations. Unless stated otherwise, the physics list set in Geant4 is QBBC. This list was developed for simulations of radio medical treatment [23]. Other physical lists like FTFP BERT provide very similar results.

4.1 Transport of the Protons in Aluminum

In Geant4 we simulate a transport of a mono-energetic proton beam ($10 - 35\,\mathrm{MeV}$) through a thick aluminum brick. The aim is to investigate how does the proton energy degrade with the increasing thickness of the aluminum. The second question to be addressed is how thick the aluminum layer has to be to stop the proton with a given initial energy. Note that in our experimental setup aluminum forms the beam pipe exit window, the degrader plates, and the shielding of the Timepix.

In order to study what are the properties of the incoming protons at given depth in the aluminum, the geometry of the aluminum brick in Geant4 is described using replicas of a basic module which consists of a $100\,\mu\mathrm{m}$ thick aluminum layer followed by a $1\,\mu\mathrm{m}$ thick vacuum layer. The thin vacuum

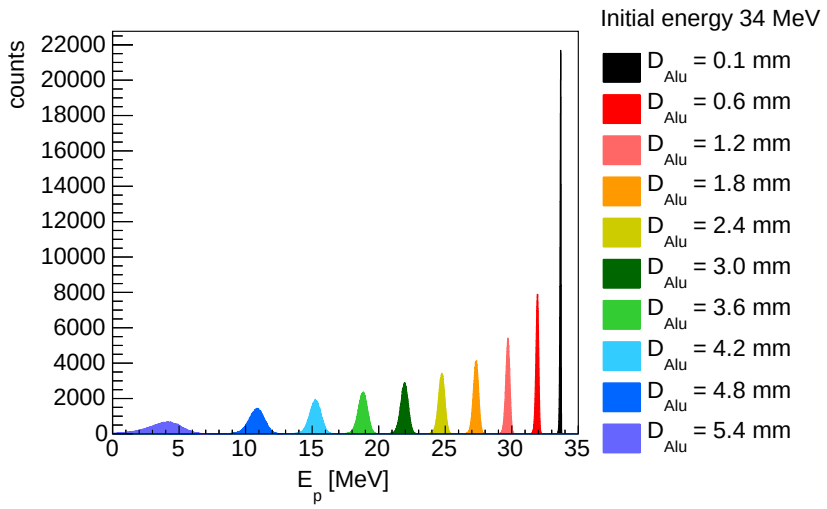

Figure 4.1: Energy spectra of protons as a function of path length traversed in aluminum (D_{Alu}). Initial beam energy is 34 MeV (mono-energetic).

layers do not affect the proton beam energy. They are used to get access to the energy of the beam protons at well defined depth in the material.

Figure 4.1 illustrates how the initial 34 MeV mono-energetic proton beam modifies after passing through an aluminum layer of given thickness. As the aluminum budget increases, the mean of the distributions shifts downwards. In addition, the distributions get wider which demonstrates the random nature of the processes involved in the mechanism of energy loss. In the left hand side panel of Figure 4.2 we plot the mean energy of the beam protons as a function of the aluminum thickness. The initial energy of the mono-energetic proton beam was varied from 10 MeV to 34 MeV. We observe that the slope of the curves gets steeper as the kinetic energy of the protons decreases. A derivative of the curves would exhibit the Bragg peak, cf. Section 1.1. Based on the data in the left hand side panel of Figure 4.2 we conclude that a 8 mm thick aluminum plate should be sufficient to stop the 35 MeV proton beam completely. In the right hand side panel of Figure 4.2 we show a ratio of proton energy RMS/mean versus the thickness of the aluminum layer. This plot illustrates the relative precision of the proton beam energy that can be achieved at given depth in aluminum.

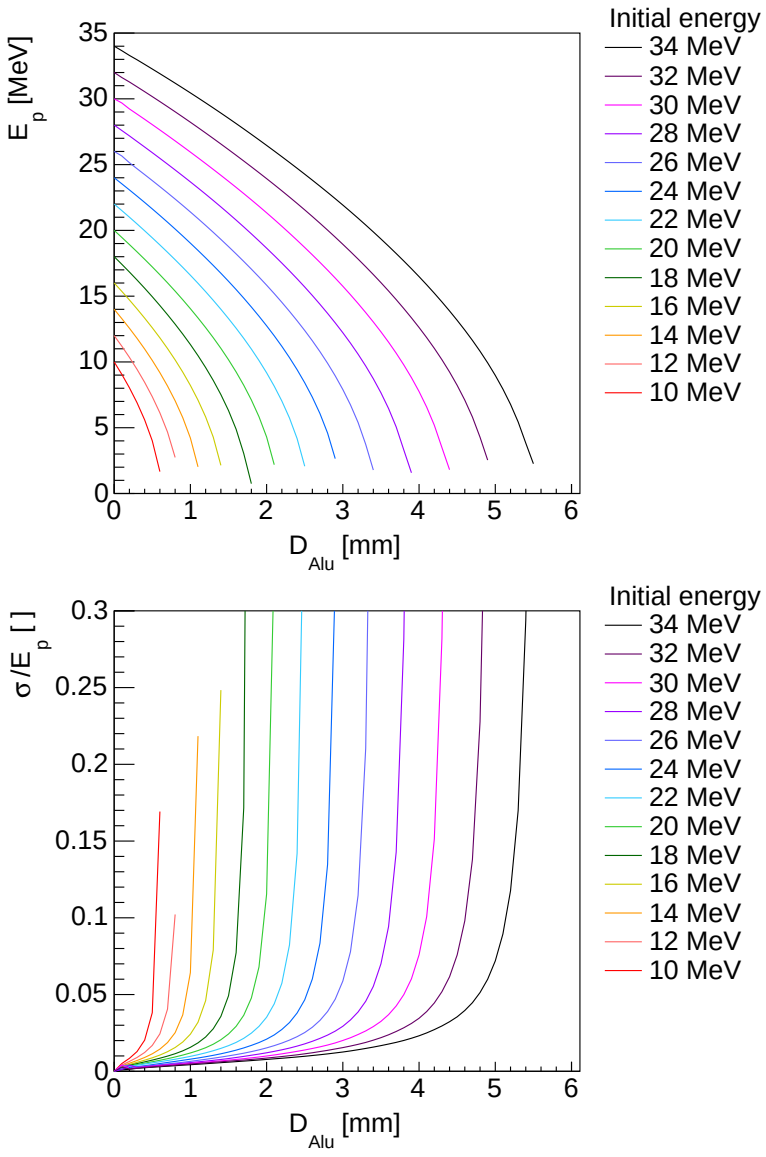

Figure 4.2: Top: Mean proton energy E_p in aluminum depth D_{Alu} for initial proton energy $10-34\,\mathrm{MeV}$ simulated in Geant4. Bottom: Relative beam width to proton energy in aluminum depth for initial proton energy $10-34\,\mathrm{MeV}$ simulated in Geant4.

4.2 Transport of the Protons in Air

When the protons leave the beam pipe exit window they need to fly $\sim$ 130 cm in air before reaching the detectors. Therefore, in this section we use Geant4 to simulate how the distance traversed by the protons in air changes the proton beam energy. The simulation closely follows what was done in the previous section. The initial beam is again mono-energetic. The beam parameters are monitored in 2 cm steps. In Figure 4.3 we show the mean energy of the protons as a function of the distance traveled in air. When compared to Figure 4.2 we see that the stopping power in air is much smaller when compared to the aluminum. Within a quite broad energy range of the initial beam energies the stopping power seems to be with a good accuracy ~ 2 MeV/m.

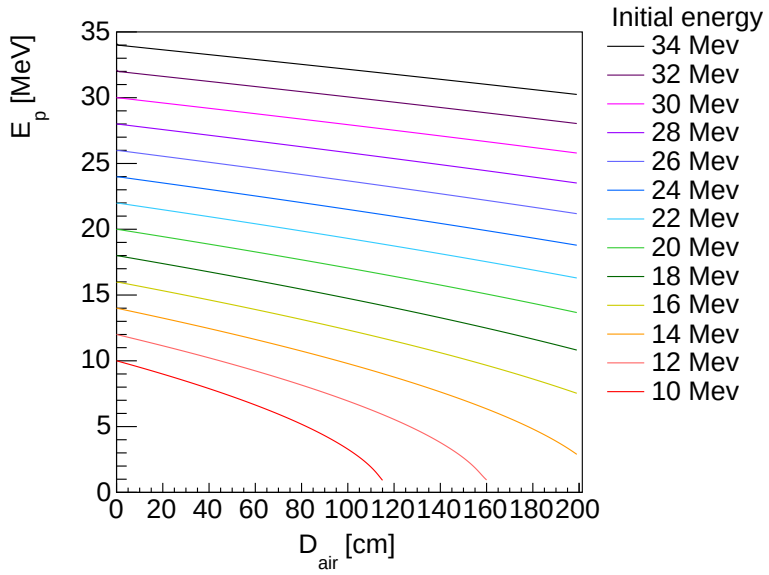

Figure 4.3: Mean proton energy E_p in air depth D_{air} for initial proton energy $10 - 34$ MeV simulated in Geant4.

4.3 Timepix in Vacuum

In this section we investigate how large energy depositions are induced by mono-energetic protons in the Timepix. The geometry of the Timepix was described as a 300 μm thick silicon box placed in vacuum. Since the simulated geometry is particularly simple it allows to make a direct comparison between the simulations by Geant4 and SRIM. The mean proton energy deposition in

the Timepix as a function of the initial beam energy is shown in Figure 4.4. We observe that Geant4 and SRIM provide consistent predictions.

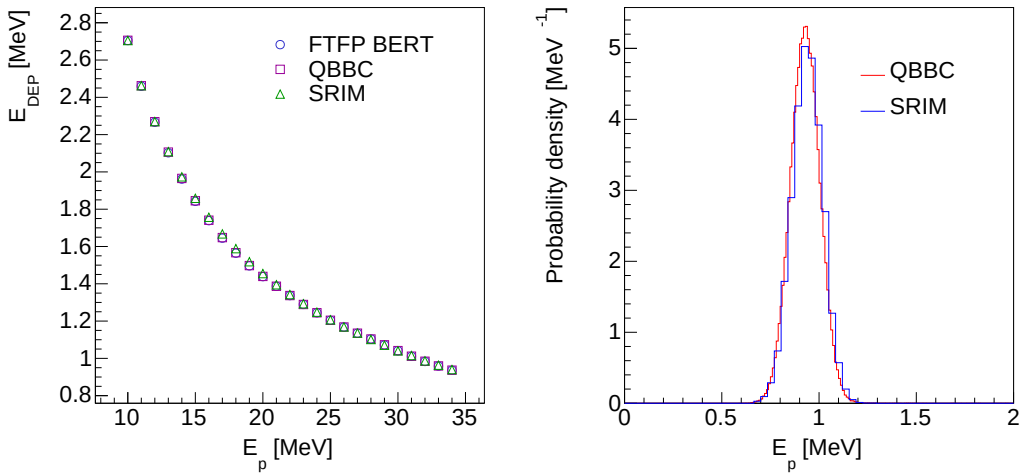

Figure 4.4: Left: Energy deposition E_{DEP} in semiconductor silicon layer of Timepix chip for different initial proton energy E_p simulated in Geant4 with QBBC physics list and FTFP BERT physics list. Right: Distribution of energy deposition in 300 μm thick silicon by a proton with energy 34 MeV simulated in SRIM and Geant4 with QBBC physics list.

4.4 Ionization Chamber in Vacuum

Figure 4.5: Geometry of the ionization chamber simulated in Geant4. The radius of the layers is taken form dimensions guaranteed by manufacturer in Figure 2.7.

Similarly to the previous section, here we study how large energy deposition are left by mono-energetic protons in the ionization chamber. The simulation was done using Geant4. In the simulation, the ionization chamber was surrounded by vacuum. Its geometry was a bit simplified w.r.t. the technical

drawing in Figure 2.7. The chamber was considered to consist of 21.2 mm long coaxial tubes of PMMA, graphite, air and aluminum, see Figure 4.5. The inner and outer radii of the tubes were set according to the dimensions given in Figure 2.7. The sensitive volume of the chamber is the air layer. In Figure 4.6 we present the mean proton energy deposition in this sensitive volume as a function of the initial proton energy. The distribution exhibits a clear peak at $\sim$ 16 MeV. The peak is caused by the protons that pass through the central aluminum wire. The $\sim$ 16 MeV protons lose in the wire just enough energy that the maximum of stopping power (Bragg peak) is reached in the air layer behind the wire. This claim was verified by a simulation in which the aluminum electrode was omitted and where the peak does not occur.

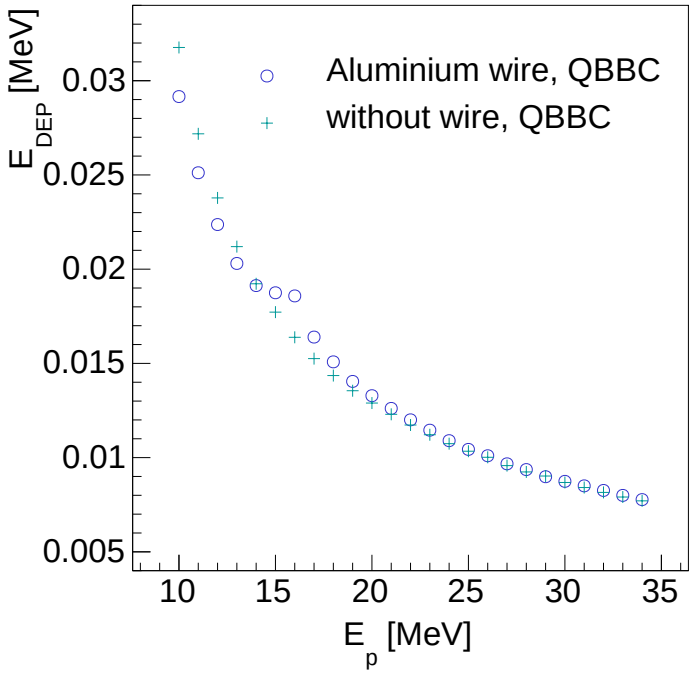

Figure 4.6: Energy deposition E_{DEP} in the ionization chamber working gas for different initial proton energy E_p simulated in Geant4 with and without aluminum electrode wire with the QBBC physics list.

4.5 Simulation of the Setup

In this section, we employ Geant4 and SRIM to simulate a simplified geometry of the experimental setup, cf. Section 2.5. The projectile protons have 34.858 MeV and they are mono-energetic. They pass through 55 μm thick aluminum beam pipe exit window, fly through 130 cm of air and hit the detector

(Timepix or the ionization chamber). The geometry can be modified by inserting degrader aluminum plates. The thickness of the plates is taken from Table 2.2. Their positions w.r.t. the beam pipe exit window are taken from the experiment. A scheme of the simulated geometry (with three degrader plates in the beam) is shown in Figure 4.7.

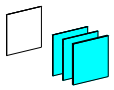

Figure 4.7: Geometry of the full setup simulated in Geant4. From left to right we see the beam pipe exit window, three degrader plates and the ionization chamber. The proton beam comes from the upper left corner.

The first question to be addressed with the simulation concerns the energy spectrum of the protons which are just about to hit our detectors. In Figure 4.8 we show what isthe proton energy spectrum in front of the Timepix detector as a function of the total thickness of the aluminum degrader plates placed in the beam.

The second problem to be addressed concerns the distribution of the energy left by the protons in the Timepix. Recall, that the TOT measured by the Timepix can be related to the energy deposition, cf. (2.5). This allows us to crosscheck whether the energy deposition by the proton in the Timepix chip calculated with Geant 4 and SRIM reproduces the measured data, see Figure 4.9. The measured distribution of the energy deposition induced by one proton is obtained from the single proton clusters (cf. Section 3.4). The distribution has a form of a peak sitting on top of a continuum. The peak is formed by the clusters where the Timepix electronics managed to collect all the charge liberated by the proton energy deposition in silicon. The continuum below the peak is a background which comes from the clusters where the charge collection was completed only partially or when there was a merging of unresolved clusters. Comparing the positions of the peak in Geant4, SRIM and the measured data we see quite a good agreement. Geant4 and SRIM tend to underestimate the mean of the energy deposition by about 10%. Geant4 gives more realistic width of the peak. Finally, we come to the question whether it is possible to get the quantitative understanding of the measured calibration

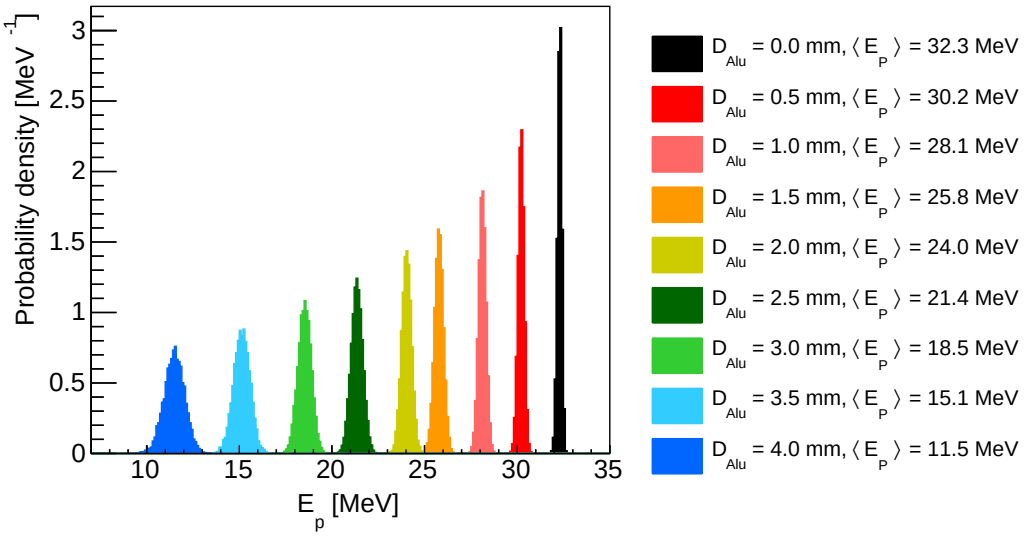

Figure 4.8: Energy spectra of protons in front of the Timepix detector for different degrader configurations. The initial beam energy is 34.850 MeV.

curves in Figure 3.26 based on the information provided by Geant4.

Lets us suppose a simple model of the ionization current measured by the chamber. Since the electron mobility in gas is typically much larger than the mobility of ions we will assume that the ionization current is created by the electrons only. Each electron carries one elementary charge e. The mean number of electrons that are created on average from a given energy deposition E_{dep} in air equals

$$N_{pairs} = \frac{E_{dep}}{\varepsilon} \tag{4.1}$$

where ε denotes the mean energy needed to produce one electron-ion pair in the air, $\varepsilon = 34\,\mathrm{eV}$ [13, 8, 11]. The Geant4 simulation then gives us the mean energy deposition $\left\langle E_{dep} \right\rangle$ left by one proton in the sensitive volume of the chamber,see Figure 4.10. Assuming a homogeneous beam profile, the mean number of protons per second that traverse the ionization chamber is equal to the product of the proton flux ϕ and the cross section A of the chamber exposed to the incoming beam. Hence, the ionization current can be expressed as

$$I = e \cdot \frac{\left\langle E_{dep} \right\rangle}{\varepsilon} \cdot A \cdot \phi, \tag{4.2}$$

where $A = 2.12 \times 0.61\,\mathrm{cm}^2$, cf. Figure 2.7. Comparing (4.2) and (3.11), the constant k could be written as

$$k = \frac{\varepsilon}{\left\langle E_{dep} \right\rangle \cdot e \cdot A}\,. \tag{4.3}$$

In Figure 4.11, Figure 4.12 and Figure 4.12 we compare the prediction of the formula (4.2) with the measured data. We observe that our simple-minded model provides quite a good description of the measured dependence. However, the ionization current calculated for a given size of ϕ seems to be systematically smaller. This discrepancy can have various reasons, e.g., under-estimated energy depositions by Geant4, neglected ionization current induced by ions, incomplete description of the chamber geometry in Geant4 etc. Thus we can conclude, that we have reached the quantitative understanding of the measured calibration curves in Figure 3.26 within 30%.

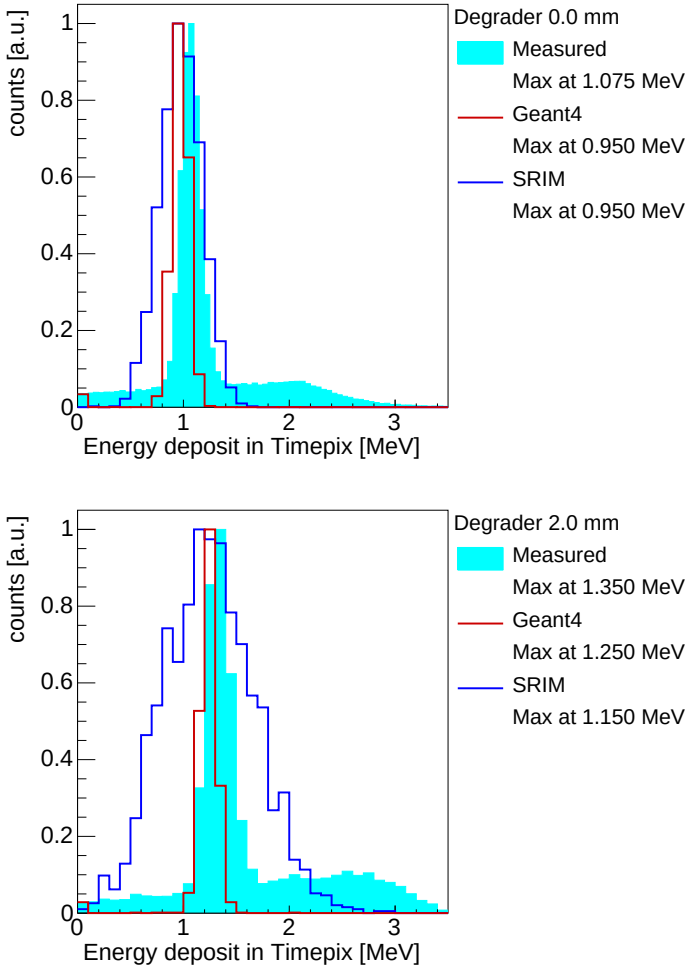

Figure 4.9: Distribution of energy deposition left by single protons in the Timepix. The energy of incident protons is modified by changing the configuration of degrader plates placed to the beam. Top panel: no plate in the degrader (proton energy in front of the Timepix is $\approx 32.3\,\mathrm{MeV}$, cf. Figure 4.8) Bottom panel: 2 mm aluminum plate in the beam (proton energy $\approx 24\,\mathrm{MeV}$). There is a clear difference between the mean of the distribution in the measured data and simulation. We quantify this difference by quoting the position of the bin with the maximum number of counts.

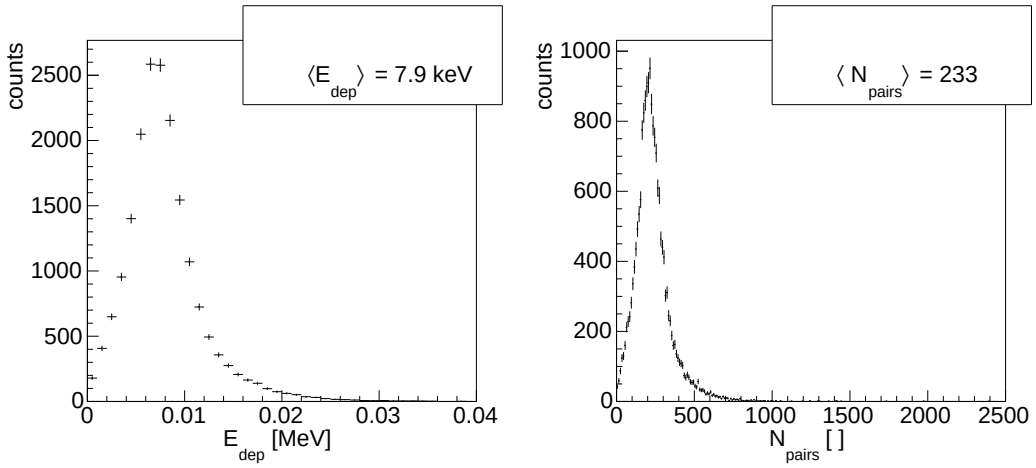

Figure 4.10: Left: Energy deposition of 34.858 MeV protons in the sensitive volume of the ionization chamber. Right: The corresponding number of electron-ion pairs generated in the air inside the ionization chamber. The Geant4 simulation is done with the QBBC physics list without any degrader plates in the beam trajectory.

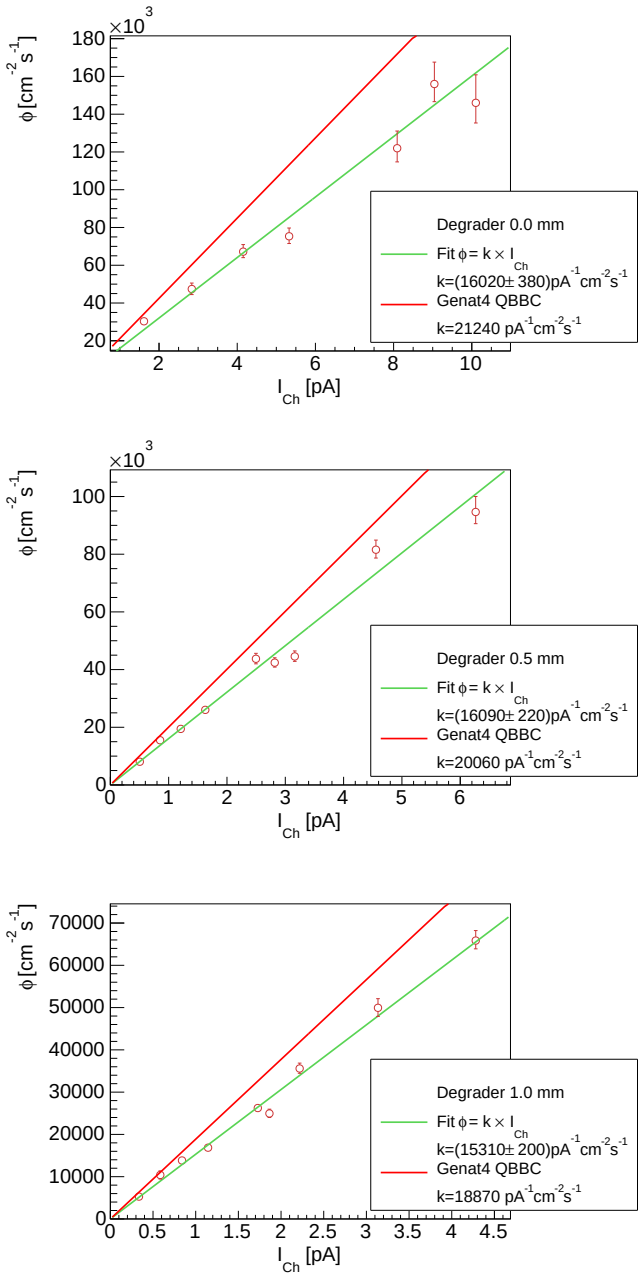

Figure 4.11: The measured ionization chamber current I_{ch} as a function of the proton flux ϕ determined from the analysis of Timepix frames. The data are fitted with linear functions $\phi = k \cdot I_{ch}$, where the slope parameter k of the green line is obtained form the fit to the data. The red line is obtained from equation (4.3) which is based on the Geant4 simulations. Thickness of the aluminum plates placed in the beam is 0.0 mm, 0.5 mm, 1.0 mm.

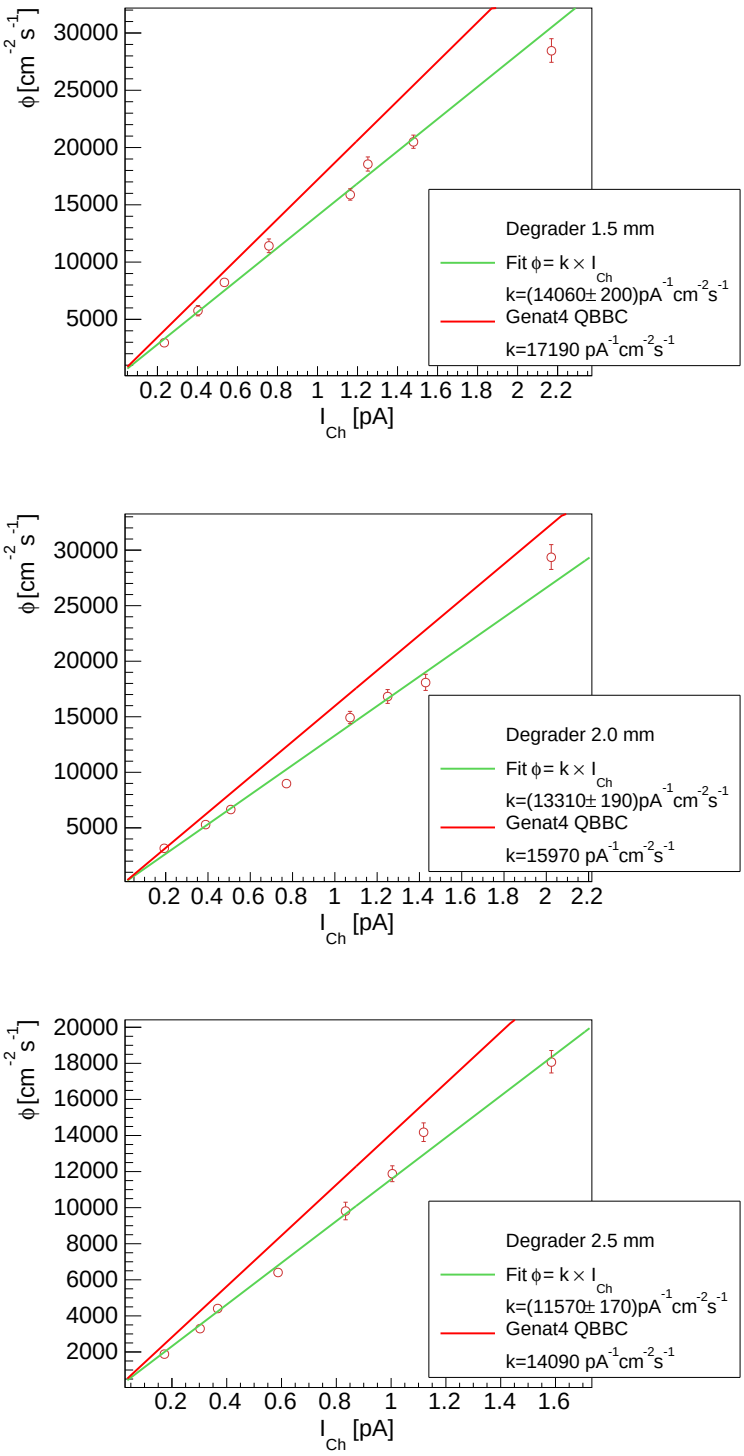

Figure 4.12: The same as Figure 3.22. Thickness of the aluminum plates placed in the beam is 1.5 mm, 2.0 mm, 2.5 mm.

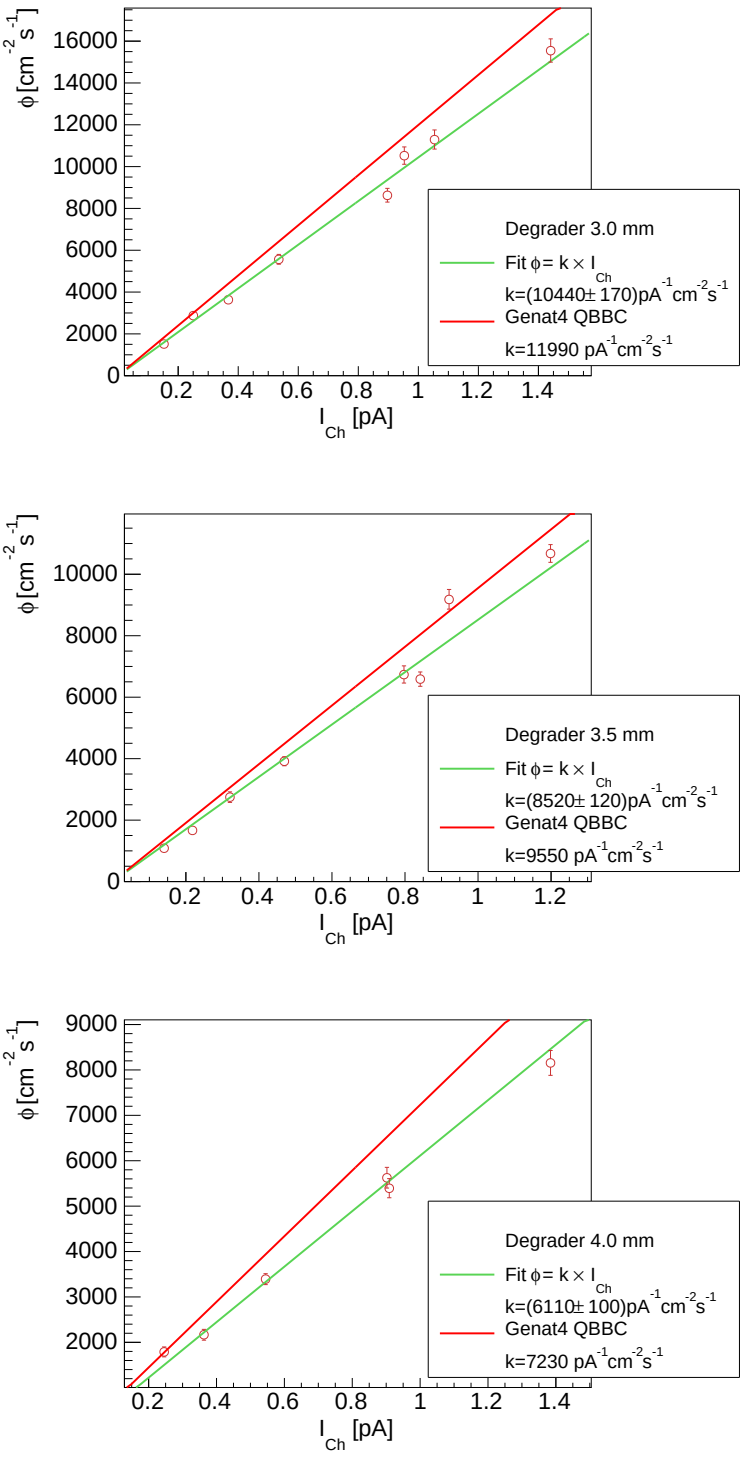

Figure 4.13: The same as Figure 3.22. Thickness of the aluminum plates placed in the beam is 3.0 mm, 3.5 mm and 4.0 mm.

Chapter 5

Conclusion

The upgrade project of the ALICE ITS detector requires to perform a series of radiation hardness tests of the various components to be used in the new system. The Czech ALICE group uses for this purpose the proton fluxes delivered by the isochronous cyclotron U-120M. The components that have been irradiated so far are, e.g. FPGAs and cables. These tests will help the ALICE collaboration to come up with a reliable, radiation tolerant detector system which will have stable performance over the whole period of operation.

In this thesis I elaborate the on-line beam monitoring techniques that are used during the tests of radiation hardness at the U-120M cyclotron. The main goal of the thesis was to provide the calibration curves that allow to convert the ionization current measured by the ionization chamber 30010 PTW to the instantaneous proton flux. The calibration curves that I obtained are shown in Figure 3.26. They exhibit a manifestly linear correlation between the current measured by the chamber and the proton flux measured by the Timepix. This is in agreement with the expected behavior guaranteed by the manufacturer.

In an independent analysis, that is not a part of this thesis, FNSPE students Zlata Tabachová and Valentina Raskina investigated whether the obtained calibration curves hold at much larger ionization currents. Figure 5.1 compares our calibration curve with a measurement of the proton flux obtained by means of the activation analysis which they performed. The experimental setup for the activation analysis was the same as for our measurement, i.e., the chamber and the copper activation foils were displaced 130 cm from the beam pipe exit window. The protons had an energy of 34.85 MeV. In the activation analysis they examined the yields of the reactions ^{nat}Cu(p,X)^{62}Zn and ^{nat}Cu(p,X)^{63}Zn. Based on the measured yield of the ^{63}Zn and ^{62}Zn isotopes and the known reaction cross section they estimated the proton flux using (1.7) . The Figure 5.1 demonstrates that the obtained calibration curve can be extrapolated up to the ionization currents of about 100 nA (i.e. currents that are five orders of magnitude greater than the currents used for the calibration) where it still

gives a very good description of the experimental data. For $I_{ch} > 100\,\mathrm{nA}$ we observe deviations of the measured data from the linear trend. These are probably caused by the saturation of the ionization current in the chamber.

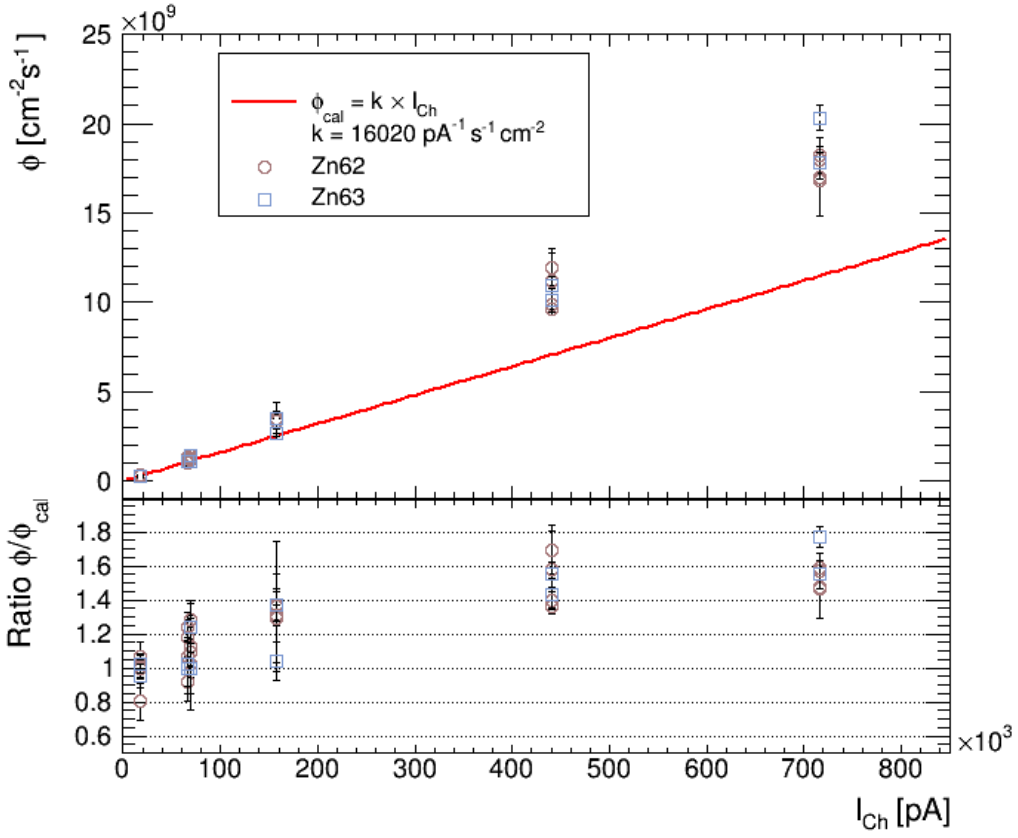

Figure 5.1: Proton flux obtained by the activation analysis versus the ionization current measured by the chamber. The results from the reactions $^{\mathrm{nat}}$Cu(p,X)^{62}Zn and $^{\mathrm{nat}}$Cu(p,X)^{63}Zn are shown separately. The red line marks the calibration curve obtained in this analysis. There was no degrader plate in the beam. Taken from [40]

In order to have a better understanding of various kinds of phenomena that are observed during proton irradiation I gave a brief overview of the basics of proton interaction in matter. In addition I have performed some simple Geant4 and SRIM simulations to deepen our understanding of the proton detection by means of the ionization chamber and the Timepix.

The performed simulations study the energy spectrum of the proton beam in the aluminum and air, the main contributors to the material budget of our setup. This study is important because the path traversed by the beam through the aluminum plates and air affects the proton beam properties before it hits the detectors.

In the Timepix as well as in the ionization chamber the detector response is proportional to the energy deposited in the sensitive volume of the detector. Therefore I examined how large energy depositions are left by mono-energetic protons in the Timepix and the ionization chamber.

Finally, I have performed a simulation of the full setup. Namely, I compared the measured proton energy depositions in the Timepix chip with the calculations by SRIM and Geant4. The results show that the simulations tend to underestimate the deposited energy by about 10 %. Moreover, I have tried to explain the slope of the measured calibration curves based on a simulation of the energy deposition and the expected electron-ion pair production in the sensitive volume of the ionization chamber. The slopes of the calibration curves obtained based on the naïve formula (4.3) are about 30% systematically smaller than the measured ones. This discrepancy can have various reasons, e.g., underestimated energy depositions by Geant4, neglected ionization current induced by ions, incomplete description of the chamber geometry in Geant4 etc.

The presented work can be extended in future. On the experimental side it would be beneficial to elaborate the measurement of high proton fluxes in the region where we observe the saturation of the ionization chamber current. Or one could study how different ways to reduce the proton beam intensity discussed in section 2.1 affect the beam profile. Concerning the simulations there is a room to improve the description of the ionization chamber geometry, to take into account atmospheric conditions mentioned in section 3.1 or to study how the uncertainty of the degrader plate widths influences the obtained results. In addition one may try to use different physics lists provided by Geant4 to run the simulations.

Appendices

Appendix A

Supplement for Chapter 2

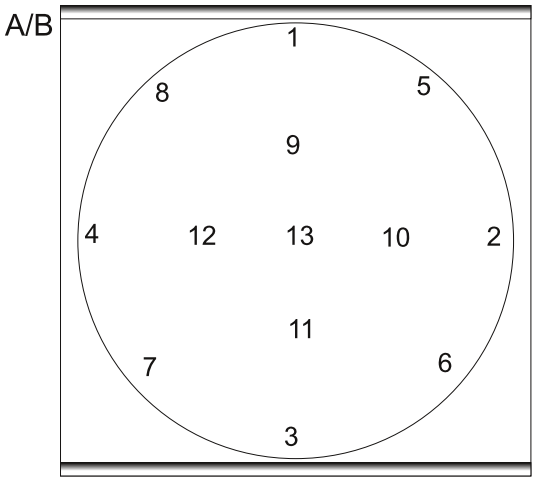

Figure A.1: Scheme of a degrader plate with marked points where the measurements of thickness were done.

N [-]	d_{A5} [mm]	d_{B5} [mm]	d_{A4} [mm]	d_{B4} [mm]	d_{A3} [mm]	d_{B3} [mm]	d_{A2} [mm]	d_{B2} [mm]
1	4.18	3.86	2.08	1.90	1.08	0.82	0.53	0.46
2	4.20	3.90	2.03	1.94	1.08	0.84	0.52	0.49
3	4.20	3.86	2.07	1.92	1.07	0.85	0.52	0.48
4	4.22	3.91	2.04	1.93	1.09	0.83	0.52	0.46
5	4.19	3.89	2.05	1.91	1.08	0.83	0.52	0.47
6	4.19	3.90	2.06	1.92	1.08	0.84	0.52	0.49
7	4.21	3.88	2.07	1.91	1.07	0.83	0.52	0.49
8	4.18	3.90	2.03	1.92	1.08	0.83	0.53	0.45
9	4.18	3.87	2.04	1.91	1.11	0.89	0.64	0.51
10	4.19	3.89	2.04	1.92	1.11	0.88	0.63	0.51
11	4.19	3.87	2.04	1.91	1.11	0.88	0.63	0.50
12	4.20	3.88	2.04	1.92	1.12	0.90	0.64	0.50
13	4.19	3.88	2.04	1.91	1.12	0.91	0.67	0.51

Table A.1: The thickness of the degrader aluminum plates measured at different positions N, see Figure A.1, for set A and B

U[V]	I[pA]	I[pA]	I[pA]	I[pA]	I[pA]
400	0.155±0.020	10.3±0.3	20.1±0.3	50±3	100±5
350	0.155±0.020	9.7±0.3	20.2±0.3	48±2	105±5
300	0.155±0.020	9.3±0.5	20.7±0.3	51±3	101±5
250	0.155±0.020	9.7±0.5	19.9±0.3	55±5	101±5
200	0.155±0.020	10.0±0.3	19.9±0.3	48±5	99±5
150	0.150±0.020	10.2±0.3	20.0±0.5	50±3	97±5
100	0.150±0.020	10.1±0.3	20.0±0.3	50±3	105±5
50	0.145±0.020	10.1±0.3	21.1±0.5	51±3	110±10

Table A.2: Ionization chamber current I versus the voltage U set on the chamber. The data in columns correspond to different proton beam intensities.

Bibliography

[1] Dominique Brière and Pascal Traverse. AIRBUS A320/A330/A340 Electrical Flight Controls: A Family of Fault-Tolerant Systems. In *Symposium on Fault-Tolerant Computing*, pages 616–623, 1993.

[2] The ALICE Collaboration. The ALICE experiment at the CERN LHC. *Journal of Instrumentation*, 3, August 2008.

[3] Serhiy Senyukov. The upgrade of the ALICE Inner Tracking System. *Nucl. Instrum. Meth.*, A732:164–167, 2013.

[4] Department of accelerators. Isochronous cyclotron U-120M. http://accs.ujf.cas.cz. [Online; accessed 17-December-2015].

[5] T. Vanat, J. Pospisil, F. Krizek, J. Ferencei, and H. Kubatova. A System for Radiation Testing and Physical Fault Injection into the FPGAs and Other Electronics. In *Digital System Design (DSD), 2015 Euromicro Conference on*, pages 205–210, August 2015.

[6] PTW ®. Farmer ionization chambers. http://www.ptw.de /farmer_chambers0.html. [Online; accessed 4-January-2016].

[7] X. Llopart, R. Ballabriga, M. Campbell, L. Tlustos, and W. Wong. Timepix, A 65k programmable pixel readout chip for arrival time, energy and/or photon counting measurements . *Nuclear Instruments and Methods in Physics Research Section A: Accelerators, Spectrometers, Detectors and Associated Equipment*, 581(1–2):485 – 494, 2007. {VCI} 2007Proceedings of the 11th International Vienna Conference on Instrumentation.

[8] W.R. Leo. *Techniques for Nuclear and Particle Physics Experiments: A How-to Approach*. Springer, 1994.

[9] H. A. Bethe, F. Low, K. M. Watson, R. Jastrow, F. J. Dyson, and G. Wentzel. Theoretical calculations of pion-nucleon scattering. In *Proceedings, 3rd Annual Rochester Conference on High Energy Nuclear Physics (ICHEP 52 - Rochester)*, pages 74–88, 1953.

[10] K. A. Olive et al. Review of Particle Physics. *Chin. Phys.*, C38:090001, 2014.

[11] C. Leroy and P.G. Rancoita. *Principles of Radiation Interaction in Matter and Detection*. World Scientific, 2009.

[12] Particle therapy cancer research institute. https://www.ptcri.ox.ac.uk/research/introduction.shtml. [Online; accessed 3-January-2016].

[13] L. Musílek. *Úvod do fyziky ionizujícího záření*. Populární přednášky o fyzice. SNTL, 1979.

[14] Stefano Meroli. Multiple scattering for particles in the matter. http://meroli.web.cern.ch/meroli/lecture_multiple_scattering.html. [Online; accessed 5-January-2016].

[15] E. Keil, E. Zeitler, and W. Zinn. Single and plural scattering of charged particles. *UCRL-TRANS-1036*, 1960.

[16] Yung-Su Tsai. Pair production and bremsstrahlung of charged leptons. *Rev. Mod. Phys.*, 46:815–851, Oct 1974.

[17] G. Moliere. Theorie der Streuung schneller geladener Teilchen I. Einzelstreuung am abgeschirmten Coulomb-Feld. *Z. Naturforsch.*, A2:133, 1947.

[18] A. O. Hanson, L. H. Lanzl, E. M. Lyman, and M. B. Scott. Measurement of Multiple Scattering of 15.7-Mev Electrons. *Phys. Rev.*, 84:634–637, Nov 1951.

[19] Recommended cross sections for 27Al(p,x)22Na reaction . https://www-nds.iaea.org/medical/alp22na0.html. [Online; accessed 20-December-2015].

[20] A. McNair. Icru report 33 - radiation quantities and units pub: International commission on radiation units and measurements, washington d.c. usa issued 15 april 1980, pp.25. *Journal of Labelled Compounds and Radiopharmaceuticals*, 18(9):1398–1398, 1981.

[21] Marie Davídková. private communication, 2014.

[22] James F. Ziegler and Jochen P. Biersack. The Stopping and Range of Ions in Matter. In D.Allan Bromley, editor, *Treatise on Heavy-Ion Science*, pages 93–129. Springer US, 1985.

[23] S. Agostinelli et al. GEANT4: A Simulation toolkit. *Nucl. Instrum. Meth.*, A506:250–303, 2003.

[24] Ernest O. Lawrence. Method and apparatus for the acceleration of ions, February 20 1934. US Patent 1,948,384.

[25] Wikipedia. Cyclotron — wikipedia, the free encyclopedia. https://en.wikipedia.org/wiki/Cyclotron, 2015. [Online; accessed 21-December-2015].

[26] Jan Štursa. private communication, 2014.

[27] Tomáš Vaňát. private communication, 2014-2015.

[28] EQUIPCO. Introduction to radiation detectors. http://www.equipcoservices.com/support/tutorials/introduction-to-radiation-monitors/. [Online; accessed 27-December-2015].

[29] UNIDOS E ®. Universal dosemeter. http://www.ptw.de/unidos_e_dosemeter_ad0.html. [Online; accessed 30-December-2015].

[30] User Manual. Ionization Chamber Type 30010, 30011, 30012, 30013. D596.131.00/03 2006-09 Hn, Freiburg: PTW, 2013. 16.

[31] MEDIPIX. The Timepix Chip. https://medipix.web.cern.ch/medipix/pages/medipix2/timepix.php. [Online; accessed 23-December-2015].

[32] Michal Platkevič. Medipix 2. http://147.32.68.57/ofat/others/Medipix2/index.html. [Online; accessed 23-December-2015].

[33] MEDIPIX. Medipix collaboration. https://medipix.web.cern.ch/medipix/index.php. [Online; accessed 24-December-2015].

[34] Radionuclide safety data sheet. Nuclide: Hg203. http://web.stanford.edu/dept/EHS/prod/researchlab/radlaser/RSDS_sheets/Hg-203.pdf. [Online; accessed 1-January-2016].

[35] The LANG positioning system. MCL. http://www.lang.de/product-overview/automation-systems/positioning-systems/mcl.html. [Online; accessed 3-January-2016].

[36] Cyclotron crew. private communication, 24. and 25. 11. 2014.

[37] CEM instruments. http://www.cem-instruments.com/en/pro/ pro-292.html, 2015.

[38] M Kroupa, S Hoang, N Stoffle, P Soukup, J Jakubek, and L S Pinsky. Energy resolution and power consumption of Timepix detector for different detector settings and saturation of front-end electronics. *Journal of Instrumentation*, 9(05):C05008, 2014.

[39] Martin Ovesný, Pavel Křížek, Josef Borkovec, Zdeněk Švindrych, and Guy M. Hagen. ThunderSTORM: a comprehensive ImageJ plug-in for PALM and STORM data analysis and super-resolution imaging. *Bioinformatics*, 30(16):2389–2390, 2014.

[40] Zlata Tabachova and Valentina Raskina. private communication, 2015.